

# Optical Design: from Extreme Ultraviolet Lithography to Thermo-Photovoltaics

*Greggory Scranton*



Electrical Engineering and Computer Sciences  
University of California at Berkeley

Technical Report No. UCB/EECS-2017-227

<http://www2.eecs.berkeley.edu/Pubs/TechRpts/2017/EECS-2017-227.html>

December 15, 2017

Copyright © 2017, by the author(s).  
All rights reserved.

Permission to make digital or hard copies of all or part of this work for personal or classroom use is granted without fee provided that copies are not made or distributed for profit or commercial advantage and that copies bear this notice and the full citation on the first page. To copy otherwise, to republish, to post on servers or to redistribute to lists, requires prior specific permission.

Optical Design: from Extreme Ultraviolet Lithography to Thermo-Photovoltaics

By

Greggory Scranton

A dissertation submitted in partial satisfaction of the

requirements for the degree of

Doctor of Philosophy

in

Engineering – Electrical Engineering and Computer Sciences

in the

Graduate Division

of the

University of California, Berkeley

Committee in charge:

Professor Eli Yablonovitch, Chair

Professor Ming C. Wu

Professor Per Peterson

Fall 2017

Optical Design: from Extreme Ultraviolet Lithography to Thermo-Photovoltaics

© Copyright 2017

Greggory Scranton

All rights reserved

To my Parents

## Abstract

Optical Design: from Extreme Ultraviolet Lithography to Thermo-Photovoltaics

by

Greggory Scranton

Doctor of Philosophy in Engineering—Electrical Engineering and Computer Science

University of California, Berkeley

Professor Eli Yablonovitch, Chair

As optics and photonics technologies advance, more energy efficient use of light will be necessary. This dissertation presents methods developed to enhance the efficiency of three different optical systems: extreme ultraviolet lithography, a hybrid solar photovoltaic/thermal collection system, and thermo-photovoltaics.

Extreme ultraviolet (EUV) lithography is the leading contender to become the next industrial scale lithography technology in the semiconductor industry. Traditionally, aberration correction in extreme ultraviolet projection optics requires the use of multiple lossy mirrors, which results in prohibitively high source power requirements. This dissertation analyzes a single spherical mirror projection optical system where aberration correction is built into the mask itself through an adjoint-based optimization algorithm. This greatly reduces the power requirements for the source.

Hybrid solar photovoltaic/thermal systems offer a way to convert sunlight into electricity and heat that efficiently uses different parts of the solar spectrum. Highly efficient hybrid solar photovoltaic/thermal systems are enabled by recent advances in photovoltaic technology. Record breaking photovoltaic cells have highly reflective rear mirrors to maximize luminescence efficiency. This reflectivity can also be used to create reflective optics to concentrate the reflected radiation onto a thermal absorber. This dissertation reports on a hybrid solar photovoltaic/thermal system with a thermal efficiency of 37% at a maximum absorber temperature of 365°C, and a direct solar to electric efficiency of 8%.

Thermo-photovoltaics offers a method to use photovoltaic cells to efficiently convert heat to electricity. In a thermo-photovoltaic system, light is collected by photovoltaic cells from a local black body source. This dissertation reports on a thermo-photovoltaic device that recycles unused radiation from the photovoltaics with a highly reflective rear mirror. Theoretical efficiencies using this strategy are in excess of 50%. For an emitter temperature of 1207°C, this dissertation reports an experimental power conversion efficiency of 28.1%.

# Table of contents

Abstract.....	1
Table of contents.....	i
List of figures.....	iii
List of tables.....	ix
Acknowledgments.....	x
1 Introduction.....	1
1 Adjoint-based Optimization for Extreme Ultraviolet Lithography.....	2
1.1 Introduction.....	2
1.2 The Adjoint Method for Electromagnetic Design.....	2
1.3 The Adjoint Method Applied to ILT.....	3
1.3.3 Gradient with Respect to Electric Field.....	6
1.3.4 Gradient with Respect to Mask Transmission Factor.....	7
1.4 Results.....	10
1.4.1 Correcting Severe Spherical Aberration.....	11
1.4.2 Depth-of-Focus Optimization.....	13
1.4.3 Off-axis Aberration Correction.....	15
1.5 Angular Sensitivity Analysis.....	17
1.6 Conclusion.....	18
2 Hybrid Solar Photovoltaic and Solar Thermal Collection System.....	19
2.1 Opportunities enabled by highly reflective, high efficiency photovoltaics.....	19
2.2 Background for Hybrid Photovoltaic/Thermal Systems.....	22
2.3 Experimental Hybrid Solar Photovoltaic/Thermal System.....	23
2.4 Modeling Results.....	27
2.5 Considerations for High Temperature Photovoltaics.....	28
2.6 Experimental Results.....	30
2.7 Conclusion.....	31
4 Theory of Thermo-Photovoltaics.....	33
4.1 From Dyson Spheres to Thermo-Photovoltaics.....	33
4.2 Theoretical Efficiency.....	35

4.3	History of Thermo-Photovoltaics.....	39
5	Experiments in Thermo-Photovoltaics .....	41
5.1	Introduction .....	41
5.2	Experimental Procedure .....	41
5.3	Calorimetry.....	47
5.4	Projections and Future Work.....	48
6	Conclusion.....	52
	References .....	54

# List of figures

Figure 1 A flowchart showing one iteration in the adjoint method. First, electric and/or magnetic fields are found for the current geometry through the forward simulation. Then, the geometry gradient is found through the adjoint simulation. The gradient is used to make an update to the geometry..... 3

Figure 2 Projection optics with one mirror (a), and an equivalent system with one lens (b).  $S$  is the distance from the mirror to the mask, and  $S'$  is the distance from the mirror to the wafer (not to scale).  $D$  is the diameter of the mirror/lens..... 4

Figure 3 An example Figure-of-Merit calculation at the wafer plane. The color map shows electric field intensity. The desired pattern,  $P_d$ , is outlined by the black dashed line. The actual printed pattern,  $P_a$ , is outlined in cyan. The “error region”,  $|P_d - P_a|$ , is shown in gray. This error region is integrated to obtain the Figure-of-Merit. .... 9

Figure 4 Illumination pattern.  $\sigma_x = \sin\theta_x/NA_w$  and  $\sigma_y = \sin\theta_y/NA_w$ . These six plane waves were chosen to give the illumination some of the characteristics of an extended dipole source, such as the one outlined in black. The four  $\sigma_x$  values are -0.8182, -0.2727, 0.2727, and 0.8182. The three  $\sigma_y$  values are -0.3099, 0, and 0.3099. .... 11

Figure 5 (a) mask and (b) wafer plane intensity (normalized to clear field) for an optical system with a naïve mask and no aberrations in the on-axis position. The pattern is periodic, with one unit cell shown. The NA of the system is 0.33, the demagnification is 4, and the wavelength is 13.5 nm..... 12

Figure 6 (a) mask and (b) wafer plane intensity (normalized to clear field) for an optical system with a naïve mask in the on-axis position. The pattern is periodic, with one unit cell shown. The NA of the system is 0.33, the demagnification is 4, and the wavelength is 13.5 nm. The mirror radius is 15 cm. The image was taken at the center of the field. This naïve mask is used as the starting geometry for the optimization..... 12

Figure 7 (a) Mask and (b) wafer plane intensity (normalized to clear field) for an optical system with an optimized mask. The simulation conditions are the same as in Figure 6. With this optimized mask, all critical dimensions are within 5% of their target. . 13

Figure 8 The same optical system as in Figure 7, with the mask pixelated. The pixels are 14nm  $\times$  15 nm. All critical dimensions are within 8% of their target. .... 13

Figure 9 (a) Mask and (b) wafer plane intensity (normalized to clear field) for an optical system with a mask optimized to perform through 60nm of defocus. The simulation conditions are the same as in Figure 5. With this mask, all critical dimensions are within 7% of their target at focus, and remain within 11% through 60nm of defocus. .... 14

Figure 10 Bossung plots for the worst performing feature for the masks optimized (a) at focus, and (b) for depth-of-focus. For the mask optimized through focus, all critical dimensions remain within 11% of their targets for 60nm of defocus at nominal dose. The sharp jumps seen in the plots correspond to changes in the location of the worst performing feature. .... 14

Figure 11 A diagram showing the three points on the wafer we designed masks for. The wafer was assumed to be 33 by 26 mm. The mid-field point is displaced 6.5 mm from the optical axis and has >4000 wavelengths of coma and >230 wavelengths of astigmatism (peak value, using the convention in Equation (1.8) ). The field edge point is displaced 1.3 mm and has >9000 wavelengths of coma, and >900 wavelengths of astigmatism..... 15

Figure 12 (a) Mask and (b) wafer plane intensity (normalized to clear field) after optimization for the mid-field location 6.5mm off-axis. The mask resulting from the on-axis optimization was used as the starting mask for this optimization. All critical dimensions are within 2% of their target. .... 16

Figure 13 (a) Mask and (b) wafer plane intensity (normalized to clear field) after optimization for the field edge location 13mm off-axis. The mask resulting from the mid-field optimization was used as the starting mask for this optimization. All critical dimensions are within 3% of their target..... 16

Figure 14 A diagram showing how the angular sensitivity,  $\Delta\theta$  of an illumination plane wave depends upon the magnitude of aberration phase shift on the lens of an optical system. .... 17

Figure 15 Diagram of a solar cell at open circuit on an index-matched semiconductor substrate. Incident photons, shown in yellow, refract toward the normal upon entering the semiconductor due to the index mismatch with air. The incident photons are absorbed and re-emitted. The re-emitted photons have an energy equal to the bandgap energy of the semiconductor, and are shown in red. The re-emitted photons tend to escape into the substrate before they can build up a high light intensity. .... 19

Figure 16 Diagram of a solar cell at open circuit with a perfectly reflecting back mirror. In this case, the re-emitted photons are absorbed and re-emitted many times. This causes the light intensity to build up inside the cell. The re-emitted photons eventually escape out the front of the cell. .... 20

Figure 17 Hybrid solar photovoltaic/thermal system. Direct normal irradiance from the sun is collected by the primary reflector, a parabolic concentrating mirror. This light is concentrated onto a secondary reflector composed of gallium arsenide (GaAs) photovoltaic cells. The photovoltaic cells absorb the portion of the spectrum above their bandgap, and reflect the remaining below-bandgap light. These cells are arranged in a parabolic shape around a high temperature absorber, so that the

reflected below-bandgap light is concentrated on the absorber. The absorber contains a heat transfer fluid that is continuously pumped through it to transfer the thermal energy to where it can be harvested. .... 24

Figure 18 System components. (a) photograph of primary concentrator with structural supports for the secondary concentrator and absorber. (b) GaAs photovoltaic cell from Alta Devices. (c) Secondary concentrator and absorber inside evacuated glass tube, covered in GaAs photovoltaic cells. .... 25

Figure 19 Emissive power and emissivity of the high temperature absorber. The red curve shows the emissivity/absorptivity of the absorber (data from Himin Solar Co.). The absorber is tailored be high in the low wavelength (high photon energy) region to maximize absorption from the solar spectrum. The absorber is also tailored to have a low emissivity in the long wavelength (low photon energy) portion of the spectrum, that overlaps with most of the blackbody spectrum for a temperature of 500°C. The blue curve shows this blackbody spectrum. A low emissivity in this region prevents unwanted energy loss from the absorber via radiation. The effective emission from the high temperature absorber is shown in the green curve. .... 26

Figure 20 Photovoltaic cell and high temperature coating reflectivity verses blackbody emission and AM 1.5 solar spectrum. The red curve depicts the AM 1.5 spectrum, representing solar radiation. The blue curve depicts the reflectivity of the GaAs photovoltaic cells from Alta Devices used in the system, with constant extrapolations for the infrared and ultraviolet regions. The black curve depicts the reflectivity of the coating from Himin Solar Co. used on the high temperature absorber. The green curve depicts the black body emission from the high temperature absorber. All radiation spectra shown are normalized so that the maximum value is equal to 1.... 27

Figure 21 I-V curves for an Alta Devices GaAs solar cell at elevated temperatures under 1 sun illumination. The active area of the cell is 8.53cm<sup>2</sup> in area. Curves shown in reverse polarization, hence the negative current values. As the temperature increases, the semiconductor bandgap decreases. This has the effect of reducing the open circuit voltage, and slightly increasing the short circuit current. As the temperature increased from 25°C to 252°C, the open circuit voltage decreased from 1.08V to 0.68V, and the short circuit current increased from 234mA to 265mA. The cell area was 10cm<sup>2</sup>, so the corresponding short circuit current densities were 23.4mA/cm<sup>2</sup> and 26.5mA/cm<sup>2</sup>. Additionally, the fill factor decreased from 73.6% to 49.7%. Overall the efficiency decreased from 18.6% to 8.9%..... 28

Figure 22 Long-term experiments with an Alta Devices GaAs solar cell at elevated temperatures. (a) In this experiment, the cell was kept at 100°C under 10 sun illumination for 8 hours a day for 5 days. By the end of the experiment, the open circuit voltage and short circuit current remained the same, but the fill factor under 1 sun illumination had degraded by 3%. The 1 sun I-V curves before and after are shown here. (b) In this experiment, the same cell was kept at 150°C under 10 sun

illumination for 8 hours a day for 5 days. By the end of the experiment, the open circuit voltage and short circuit current remained the same, but the fill factor under 1 sun illumination had degraded by an additional 28%. The 1 sun I-V curves before and after are shown here. .... 29

Figure 23 Thermal efficiency for the high temperature absorber. The thermal efficiency,  $\eta_{\text{solar-thermal}}$ , is the percentage of direct normal incident light on the primary reflector that is converted into useable heat in the high temperature absorber. At the maximum output temperature of 365°C,  $\eta_{\text{solar-thermal}}$  is 37%. Most other data points are near this efficiency. At the output temperature of 330°C, there is an anomalous data point at the predicted efficiency of 47%. .... 30

Figure 24 An example of a Dyson sphere. Here, the radius of the sphere is one astronomical unit, equal to  $\sim 1.5 \times 10^{11}$  m. The sun emits a full black body spectrum at a temperature of 5777 Kelvin, and the portion of the spectrum below the bandgap of the photovoltaic cells is reflected back to the sun. .... 33

Figure 25 Thermo-photovoltaic system with reflective spectral control. In this system, a hot black body emitter is surrounded by a vacuum chamber. Photovoltaic cells lining the walls of the chamber collect light from the emitter. For high efficiency, highly reflective photovoltaic cells are used. They reflect unused radiation back to the emitter so the energy is not lost. .... 34

Figure 26 A visual representation of how the blackbody spectrum is used in a thermo-photovoltaic system with highly reflective photovoltaics. Most of the spectrum is reflected, as depicted in pink. Some of the below-bandgap radiation is parasitically absorbed by the rear mirror, as shown in the orange region labeled “mirror losses”. Most of the above-bandgap radiation is available for conversion to electricity, as shown in the blue region labeled “photovoltaic power”. If no anti-reflection coating is used, some of the above-bandgap radiation will be reflected. .... 35

Figure 27 Efficiency verses photovoltaic cell back reflectivity for Dyson spheres. A star temperature of 5777 Kelvin is assumed. A cell temperature of 20°C is assumed. The photovoltaic cell bandgap is optimized for each data point. Efficiency is calculated according to Equation (4.6). .... 37

Figure 28 Heat to electricity conversion efficiency for a thermo-photovoltaic system. In this case, the emitter temperature is 1200°C, the cell temperature is 20°C, and the external luminescence efficiency is 30%. The efficiency is 42% at a cell reflectivity of 90%. The efficiency rises above 50% at a cell reflectivity of 98%. The efficiency is 53% at a cell reflectivity of 99%. .... 38

Figure 29 Heat to electricity conversion efficiency for a thermo-photovoltaic system. In this case, the emitter temperature is 1500°C, the cell temperature is 20°C, and the external luminescence efficiency is 30%. The efficiency is 46% at a cell reflectivity

of 90%. The efficiency rises to 50% at a cell reflectivity of 95%. The efficiency is 57% at a cell reflectivity of 99%. .....	39
Figure 30 Experimental setup. A planar graphite emitter is heated by passing a large electric current through it. Beneath the emitter, a copper baffle is used to limit the area of the photovoltaic cell exposed to the illumination. The photovoltaic cell is attached to a calorimeter that keeps its temperature steady, while allowing measurements of the heat generated in the cell. For our experiment, the baffle was 1.44mm above the cell, the baffle was 1.04mm thick, and the emitter was 1.22mm above the baffle. ....	42
Figure 31 structure of photovoltaic cell. The negative side of the p n junction is on top. The active layer is n doped, and is surrounded by selective contact layers. These are surrounded by highly doped contact layers leading to gold contacts. ....	42
Figure 32 (a) Reflectivity spectrum of the InGaAs cell used in our experiment. This reflectivity spectrum was measured with a fourier transform infrared (FTIR) spectrometer. The measurement is an average over a range of angles, as the measurement was taken through a microscope objective with a numerical aperture (NA) of 0.65. The below-bandgap reflectivity is 94%, and the average above-bandgap reflectivity is 34%, owing to the lack of an anti-reflection coating. (b) External quantum efficiency of the InGaAs cell used in our experiment. The average above-bandgap value is 65%. All measurements are averaged over photon energies. ....	43
Figure 33 current-voltage curves for the InGaAs cell at different emitter temperatures. The curve for the data point with the highest efficiency is shown in red. The current density is the measured current divided by the cell's active area of 10.04mm <sup>2</sup> .....	44
Figure 34 Black body power absorbed by the InGaAs cell (blue), and electrical power extracted from the cell (red). The power absorbed is calculated by multiplying the measured reflectivity of the cell by the black body spectrum for the appropriate emitter temperature and view factor. The multiplied spectrum is then integrated. The power density is the power divided by the cell's active area of 10.04mm <sup>2</sup> . ....	45
Figure 35 Thermo-photovoltaic efficiency at different emitter temperatures. The maximum efficiency is 28.1% at an emitter temperature of 1207°C. The efficiency is defined as the electrical power extracted divided by the power absorbed by the cell. This efficiency is given by Equation (4.6) together with Eq (5.1). ....	45
Figure 36 Short circuit current density from photovoltaic cell, and resulting calculated emitter temperature. The emitter temperature was calculated from the cell's short circuit current using Equation (5.2). A small copper sample is placed on top of the emitter. When the copper sample melts, the emitter is at a temperature of 1085°C. This is used to calculate the view factor, $F_{view}=0.302$ . The current density is the measured current divided by the cell's active area of 10.04mm <sup>2</sup> .....	47

Figure 37 Calorimetry data. Absorbed power is plotted versus time. Absorbed power is calculated with Equation (5.3). Two separate calorimetry experiments were done for purposes of distinguishing between power absorbed by the cell and excess heat absorbed by the calorimeter. In one experiment, the baffle hole was covered to prevent direct illumination from entering (orange). In the other experiment, an open baffle was used with the InGaAs cell (blue). After 15 minutes, the emitter temperature was 1218°C, and the absorbed power by the cell was 137mW (1365mw/cm<sup>2</sup>). ..... 48

Figure 38 Thermo-photovoltaic efficiency projection for increasing temperature. Experimental values are shown with the circular data points. The fit used for the projection used device parameters that made the best fit to the empirical IV curve. These parameters are a series resistance of 0.47Ω, an ideality factor of 1.2, and a reverse saturation current of I<sub>0</sub>=4.398nA. .... 49

Figure 39 Efficiency projection for increasing temperatures and improved device parameters. The curve labeled “projection using empirical parameters” is the same curve shown in Figure 38. The next curve, labeled “R<sub>Series</sub>=0.1Ω”, is a projection that uses the empirical parameters with the series resistance reduced to 0.1Ω. The curve labeled “Reflectivity=99%” uses the empirical parameters, with the series resistance reduced to 0.1Ω, and the reflectivity increased to 99%. The curve labeled “external luminescence efficiency=30%” uses the empirical parameters, with the series resistance reduced to 0.1Ω, the reflectivity increased to 99%, and the external luminescence efficiency increased to 30%. ..... 51

# List of tables

Table 1 photovoltaic cell structure. The negative side of the pn junction is on top. The active layer is n doped, and is surrounded by selective contact layers. These are surrounded by highly doped contact layers leading to gold contacts. ....	43
Table 2 Experimental data on electrical characteristics and absorbed power by the photovoltaic cell at different emitter temperatures. The current density, $J_{sc}$ , and the power densities are calculated by dividing the current or power by the cell's active area of $10.04\text{mm}^2$ .....	46

# Acknowledgments

I would like to thank my advisor, Eli Yablonovitch, for his mentorship during my graduate studies. Prof. Yablonovitch has a unique perspective that emphasizes simplifying scientific ideas down to the fundamentals. This has made a wide array of scientific topics more approachable. I would also like to thank Professor Andrew Neureuther for valuable mentorship on my work in extreme ultraviolet lithography. I am also grateful to John Holzrichter, Ed Pierce, and Professor Per Peterson for providing the vital lab space and equipment for my experiments in thermo-photovoltaics.

I have had the opportunity to collaborate with many great co-workers during my time at Berkeley. I would like to thank Vidya Ganapati for laying the theoretical groundwork for my work in thermo-photovoltaics, and for passing down valuable knowledge from prior projects. Samarth Bhargava has also provided valuable insight and criticism of my work through many a conversation. Patrick Xiao has also been a valuable collaborator to bounce ideas off, and has contributed to the theory upon which this work is based. Patrick has also been a great friend outside of work. I have also collaborated with an undergraduate researcher, Simon Lorenzo, whose hard work was instrumental in obtaining experimental results. Zunaid Omair, who will be conducting future experiments, has contributed substantially in this regard as well.

I would also like to acknowledge the moral support from my friends and colleagues during my time in graduate school, including Phil Sandborn and Indrasen Bhattacharya.

# 1 Introduction

As optics and photonics technologies advance, more energy efficient use of light will be necessary. This dissertation presents methods developed to enhance the efficiency of three different optical systems: extreme ultraviolet lithography, a hybrid solar photovoltaic/thermal collection system, and thermo-photovoltaics.

Extreme ultraviolet (EUV) lithography is the leading contender to become the next industrial scale lithography technology in the semiconductor industry. Traditionally, aberration correction in extreme ultraviolet projection optics requires the use of multiple lossy mirrors, which results in prohibitively high source power requirements. If aberration correction can be achieved with a different method, this could drastically reduce the power requirements. This dissertation analyzes a single spherical mirror projection optical system where aberration correction is built into the mask itself through an adjoint-based optimization algorithm. Adjoint methods have been employed with a powerful effect in the design of optical and photonic components [13]–[20]. This dissertation explores how this method can be used to create sophisticated and unintuitive mask designs that have built-in aberration correction, circumventing the need for many lossy mirrors. The limitations of this method are then explored and enumerated.

Hybrid solar photovoltaic/thermal systems offer a way to convert sunlight into electricity and heat that efficiently uses different parts of the solar spectrum. Highly efficient hybrid solar photovoltaic/thermal systems are enabled by recent advances in photovoltaic technology. Record breaking photovoltaic cells have highly reflective rear mirrors to maximize luminescence efficiency. This reflectivity can also be used to create reflective optics to concentrate the reflected radiation onto a thermal absorber. This dissertation reports on a hybrid solar photovoltaic/thermal system that uses highly reflective GaAs cells with a bandgap of 1.4eV, nearly ideal for the solar spectrum. The system is designed for an absorber with fluid heated to 500°C. Additionally, the cooling fluid for the photovoltaic cells supplies heat at 200°C. This dissertation discusses the challenges involved in implementing such a system, determined through modelling and experimentation. The limitations of this approach are explored, and a plan for future work is developed.

Thermo-photovoltaics offers a method to use photovoltaic cells to efficiently convert heat to electricity. In a thermo-photovoltaic system, light is collected by photovoltaic cells from a local black body source. This dissertation reports on a thermo-photovoltaic device that recycles unused radiation from the photovoltaics with a highly reflective rear mirror. Similar to the hybrid photovoltaic/thermal concentrator, this is another technology enabled by record breaking highly reflective photovoltaic cells. Theoretical efficiencies using this strategy are in excess of 50%. This dissertation reports experimental results for thermo-photovoltaics using InGaAs photovoltaic cells with a bandgap of 0.74eV, nearly ideal for a black body source at a temperature near 1200°C.

# 1 Adjoint-based Optimization for Extreme Ultraviolet Lithography

## 1.1 Introduction

Extreme ultraviolet (EUV) lithography is the leading contender to become the next industrial scale lithography technology in the semiconductor industry. Nonetheless, source power requirements are a major challenge that must be overcome [1]. In EUV lithography, multiple multilayer mirrors are used instead of lenses. Since the maximum reflectivity of a single mirror is 70% [1], projection optics systems employing 6 mirrors for aberration correction transmit less than 12% of the illumination power to the wafer. To address this problem, we consider a single mirror system in which the aberration correction is built in to the mask design. This could result in  $(1-0.7^5)=83\%$  reduction in EUV source power required, but the mathematical procedure will constrain the source incoherence.

To design masks with built-in aberration correction, we employ the optimization approach called Inverse Lithography Technology (ILT), which was developed by Luminescent Inc. [2] and Intel [3]–[7], independently. This approach has the ability to explore a large design space and systematically find unintuitive, yet high-performing solutions to mask design that would not otherwise be found. We use the adjoint method, a gradient descent optimization algorithm that has great advantages over algorithms used previously for photomask design. For example, the use of gradient descent lets the algorithm converge orders of magnitude faster than non-gradient methods such as the binary search algorithm used in [8]. The adjoint method also provides more in-depth information than either the Gerchberg-Saxton algorithm in [9]–[11], or the back propagation technique in [12], allowing gradient descent to optimize more complex figures of merit.

In this report, we begin by describing the general form of the adjoint method, which has been used to successfully design of all manner of electromagnetic components [13]–[20]. We then present a specific way to apply the adjoint method to Inverse Lithography Technology. Finally, we apply this form of ILT to a single spherical mirror system with orders of magnitude greater aberrations than would ever be tolerated in a traditional multiple mirror system. The adjoint method allows us to design photomasks with non-intuitive shapes that nonetheless successfully print test patterns, in spite of these enormous aberrations.

## 1.2 The Adjoint Method for Electromagnetic Design

The adjoint method is a gradient descent optimization algorithm for designing the geometry of dielectric or metal electromagnetic devices under Maxwell's equations. Adjoint methods have been employed in the design of optical and photonic components [13]–[20] and mathematical derivations of the adjoint method are available in optimization textbooks [21], [22]. The adjoint method converges to an optimum much more rapidly than popular heuristic optimization methods such as genetic algorithms and particle swarm optimization, since it follows the gradient—the derivative of the Figure-of-Merit with respect to *all* geometric parameters.

The adjoint method calculates the gradient at all points in space within only 2 simulations, regardless of the size of the system. Absent the adjoint method,  $N$  simulations would be required to calculate the gradient using finite differences, where  $N$  is the number of geometrical parameters. For general geometry at all points in space, the adjoint method makes calculation of the gradient tractable when it would not be otherwise. For example, if a geometry is represented by a  $1000 \times 1000$  pixel grid, and each pixel is a separate parameter, the adjoint method speeds up calculation of the gradient by  $500,000\times$ . A large number of parameters is desirable because this provides more degrees of freedom to the optimizer, and hence makes a better optimum achievable.

In our implementation, the adjoint inverse solver is a small subroutine that wraps around a forward solver. This means any existing commercial Maxwell forward solver can be used.

A flowchart describing the adjoint inverse solver is shown in Figure 1. In a given iteration, the forward simulation provides the electromagnetic fields for the current geometry. Then the adjoint simulation calculates the gradient. In gradient descent, a local change in geometry is made, proportional to the calculated gradient, in preparation for the next iteration.

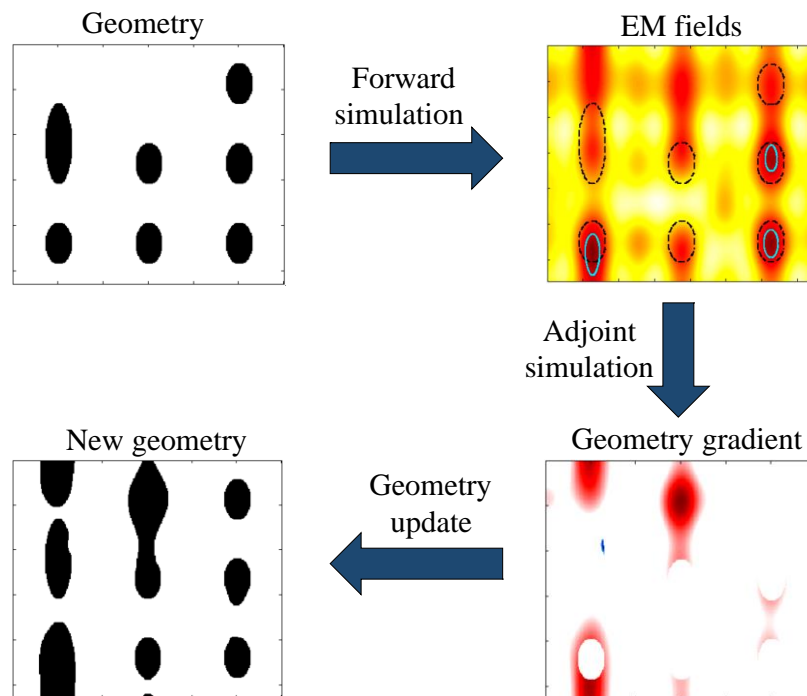


Figure 1 A flowchart showing one iteration in the adjoint method. First, electric and/or magnetic fields are found for the current geometry through the forward simulation. Then, the geometry gradient is found through the adjoint simulation. The gradient is used to make an update to the geometry.

### 1.3 The Adjoint Method Applied to ILT

This section describes our mathematical approach for applying the adjoint method to ILT for photomasks. We have adopted the mathematical formulation of the adjoint method

previously presented in [18] and [23]. These references contain a more general form of the present derivation that accounts for vector forms of both electric and magnetic fields. Only scalar electric fields are considered here.

A reflective projection optics system with one mirror is depicted in Figure 2(a). Equivalently, we model the system with a refractive lens as shown in Figure 2(b). We will find the gradient of the Figure-of-Merit (the total image error) with respect to the mask transmission factor (which defines where the mask is opaque or transmissive). The mask transmission factor is in the mask plane, while the Figure-of-Merit is a function of the electric field in the wafer plane. To find the gradient of the Figure-of-Merit, with respect to the mask transmission factor, we apply the chain rule of calculus: First find the gradient with respect to the mask plane electric field, and then the derivative of electric field with respect to the transmission factor.

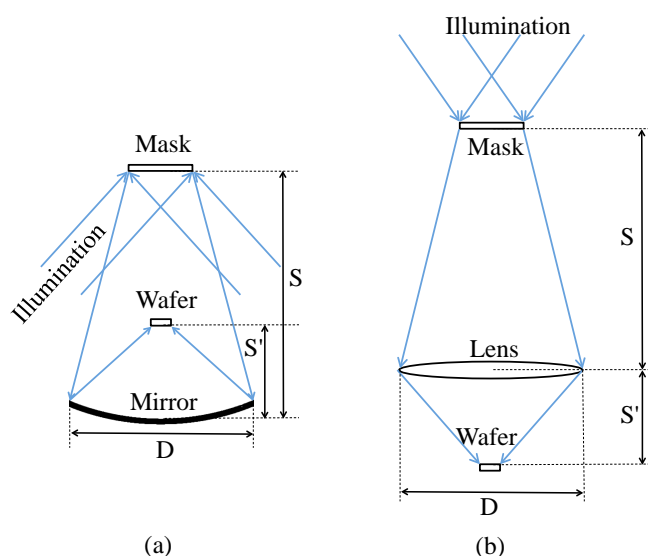


Figure 2 Projection optics with one mirror (a), and an equivalent system with one lens (b).  $S$  is the distance from the mirror to the mask, and  $S'$  is the distance from the mirror to the wafer (not to scale).  $D$  is the diameter of the mirror/lens.

### 1.3.1 Linear system model of the lithographic imaging system

Before describing our implementation of the adjoint method, the next two subsections will describe the linear system model based on the paraxial approximation used in our simulations. This model can be found in textbooks [1], [24], [25].

To simulate the projection optics, contributions to wafer intensity from different angles of illumination are considered. The electric field transmitted from the mask from one illuminating plane wave is

$$E_M(\mathbf{r}_M) = T_M(\mathbf{r}_M)E_0 \exp[ik(x_M \sin\theta_x + y_M \sin\theta_y)] \quad (1.1)$$

where  $x_M$  and  $y_M$  are the vector components of  $\mathbf{r}_M$ .  $k=2\pi/\lambda$  is the wave number of the light,  $\theta_x$  and  $\theta_y$  are each angles between the  $\mathbf{k}$  vector and a plane normal to the corresponding axis.  $T_M$  is the mask transmission factor, which is equal to 0 in absorbing regions, and 1 in transmitting regions.

To propagate this field to the wafer plane, it is convolved with the point spread function of the projection optics. The optical transfer function is the Fourier transform of the point spread function and is defined as

$$FT[PSF_{M \rightarrow W}(\mathbf{r}_M)] = OTF(\rho, \phi) = \begin{cases} \exp[-ikOPD(\rho, \phi)] & \rho \leq 1 \\ 0 & \rho > 1 \end{cases} \quad (1.2)$$

where

$$\rho = \sqrt{\left(\frac{f_x \lambda}{NA_W}\right)^2 + \left(\frac{f_y \lambda}{NA_W}\right)^2} \quad (1.3)$$

is the normalized radial coordinate,  $\phi$  is the azimuthal angle,  $f_x$  and  $f_y$  are the spatial frequencies in the x and y directions, respectively,  $NA_W$  is the numerical aperture at the wafer plane, and  $OPD$  is the optical path difference defined by the aberrations present in the system.

The intensity at the wafer plane is

$$I_W(\mathbf{r}_W) = \sum_n \left| \int_M E_{Mn}(\mathbf{r}_M) PSF_{M \rightarrow W}(\mathbf{r}_W - \mathbf{r}_M) d^2 r_M \right|^2 \quad (1.4)$$

where  $PSF_{M \rightarrow W}$  is the inverse Fourier transform of  $OTF$  in Cartesian coordinates.  $I_W$  is the sum of the intensities from each plane wave,  $E_{Mn}$ . Equation (1.4) is a modification of Equation (1.11) for a spatially incoherent system.

### 1.3.2 Aberration Wavefronts

Figure 2(a) shows a one-mirror imaging system. The relationship between radius of curvature  $R$ , mirror-to-mask distance  $S$ , and mirror-to-wafer  $S'$  is

$$\frac{1}{S'} + \frac{1}{S} = \frac{2}{R} \quad (1.5)$$

If the imaging is on-axis and the height of the mirror at the edges is ignored, the numerical aperture at the wafer plane is

$$NA_W = \frac{a}{\sqrt{a^2 + S'^2}} \quad (1.6)$$

where  $NA_W$  is the numerical aperture at the wafer, and  $NA_M$  is the numerical aperture at the mask, and  $a$  is the lateral radius of the mirror ( $a=D/2$  from Figure 2). The magnification of the system is

$$m = \frac{S'}{S} \quad (1.7)$$

We use Equation (1.5)-(1.7) to find the mirror dimensions  $R$ ,  $S$ , and  $S'$  from values of  $NA_W$ ,  $m$ , and  $a$ . The optical path difference due to the primary aberrations in such a system as given in chapter 4 of [26] is

$$OPD(\rho, \phi; h') = \frac{a^4}{4R} \left( \frac{1}{R} - \frac{1}{S'} \right)^2 \rho^4 + \frac{S'-R}{R^2 S'^2} a^3 h' \rho^3 \cos \phi + \frac{a^2}{R S'^2} h'^2 \rho^2 \cos^2 \phi \quad (1.8)$$

where  $\rho$  as before, is the normalized radial coordinate, equal to 1 at the edge of the aperture, and  $h'$  is the radial height in the image (wafer) plane. The three terms correspond to spherical aberration, coma, and astigmatism, respectively.

### 1.3.3 Gradient with Respect to Electric Field

The Figure-of-Merit is a sum of errors in the wafer plane image, and has the general form

$$FoM = \int_W f(E_W(\mathbf{r}_W)) d^2 r_W \quad (1.9)$$

where  $f$  represents a local error in the image at point  $\mathbf{r}_W$ , the subscript  $W$  denotes a variable in the wafer plane,  $E_W$  is the wafer plane electric field,  $\mathbf{r}_W$  is the two dimensional spatial position vector in the wafer plane, and bold face denotes a vector quantity. The local Figure-of-Merit  $f$ , is a step-like function of the local electric field  $E_W$ , which might be larger or smaller than a desired target electric field. Differentiating Equation (1.9) with respect to the mask plane electric field  $E_M$ , we obtain

$$\frac{\partial FoM}{\partial E_M(\mathbf{r}_M)} = \int_W \frac{\partial f}{\partial E_W(\mathbf{r}_W)} \frac{\partial E_W(\mathbf{r}_W)}{\partial E_M(\mathbf{r}_M)} d^2 r_W, \quad (1.10)$$

where the subscript  $M$  denotes a variable defined in the mask plane. During optimization, we adjust the mask to vary  $E_M$  to achieve the best possible image. To determine the partial derivative  $\partial E_W(\mathbf{r}_W) / \partial E_M(\mathbf{r}_M)$ , we must first express the wafer plane field in terms of the mask plane field.

$$E_W(\mathbf{r}_W) = \int_M E_M(\mathbf{r}_M) PSF_{M \rightarrow W}(\mathbf{r}_W - \mathbf{r}_M) d^2 r_M \quad (1.11)$$

Equation (1.11) is a convolution integral with the point spread function for propagation from the mask to the wafer plane,  $PSF_{M \rightarrow W}$ , which would generally require a solution of Maxwell's equations, but we use the paraxial and other approximations to determine  $PSF_{M \rightarrow W}$ . Substituting Equation (1.11) into Equation (1.10), we obtain

$$\frac{\partial FoM}{\partial E_M(\mathbf{r}_M)} = \int_W \frac{\partial f}{\partial E_W(\mathbf{r}_W)} \frac{\partial}{\partial E_M(\mathbf{r}_M)} \left[ \int_M E_M(\mathbf{r}'_M) PSF_{M \rightarrow W}(\mathbf{r}_W - \mathbf{r}'_M) d^2 r'_M \right] d^2 r_W \quad (1.12)$$

where  $\mathbf{r}'_M$  is a dummy variable for convolution.

We are interested in the derivative of the term in square brackets with respect to the variable  $E_M$  at one particular position  $\mathbf{r}_M$ . Since  $E_M(\mathbf{r}_M)$  and  $E_M(\mathbf{r}'_M)$  are independently controlled variables, the derivative with respect to  $E_M(\mathbf{r}_M)$  produces a delta function  $\delta(\mathbf{r}'_M - \mathbf{r}_M)$  and Equation (1.12) becomes

$$\frac{\partial FoM}{\partial E_M(\mathbf{r}_M)} = \int_W \frac{\partial f}{\partial E_W(\mathbf{r}_W)} [PSF_{M \rightarrow W}(\mathbf{r}_W - \mathbf{r}_M)] d^2 r_W \quad (1.13)$$

Equation (1.13) nearly looks like a convolution integral, but  $PSF_{M \rightarrow W}$  is an operator that only operates on functions defined in the mask plane, and  $\partial f / \partial E_W(\mathbf{r}_W)$  is in the wafer plane. This can be resolved by the reciprocity of Maxwell's equations, which dictates the reciprocal relation:

$$PSF_{M \rightarrow W}(\mathbf{r}_W - \mathbf{r}_M) = PSF_{W \rightarrow M}(\mathbf{r}_M - \mathbf{r}_W) \quad (1.14)$$

where  $PSF_{W \rightarrow M}$  is the point spread function for propagation from the wafer plane back to the mask plane. Plugging Equation (1.14) into Equation (1.13), we obtain

$$\frac{\partial FoM}{\partial E_M(\mathbf{r}_M)} = \int_W \frac{\partial f}{\partial E_W(\mathbf{r}_W)} PSF_{W \rightarrow M}(\mathbf{r}_M - \mathbf{r}_W) d^2 r_W \quad (1.15)$$

Equation (1.15) is indeed a convolution integral, and it is the important result that we have been seeking. It states that  $\partial f / \partial E_W(\mathbf{r}_W)$  can be treated as a source electric field and propagated from the wafer plane to the mask plane to obtain  $\partial FoM / \partial E_M(\mathbf{r}_M)$ . This is the adjoint simulation step shown on the right side of Figure 1.

For a spatially incoherent system that is modeled as a sum of coherent systems, the above procedure must be executed for every angle of illumination. Gradients of the  $FoM$  with respect to the electric field, properly weighted over the angles of illumination must be considered.

### 1.3.4 Gradient with Respect to Mask Transmission Factor

In the geometry update, changes in mask geometry must be derived from changes in mask plane electric field. In our simple model, each pixel in the mask is either perfectly opaque or perfectly transmitting. Thus, the mask is represented by a transmission factor,  $T_M$ , which has values of either 0 or 1, and multiplies the incoming field. To include mask edge effects, a more complete electromagnetic model would be required. A method for including electromagnetic effects in the optimization is described in [18] and [23]. To update the mask geometry, represented by a transmission factor  $T_M$ , the Figure-of-Merit derivative with respect to local electric field,  $\partial FoM / \partial E_M$  must be related to the derivative with respect to transmission factor  $\partial FoM / \partial T_M$ . The mask plane field is related to the mask transmission factor by

$$E_M(\mathbf{r}_M) = T_M(\mathbf{r}_M) E_0 \exp[i\phi_{EM}(\mathbf{r}_M)] \quad (1.16)$$

Where  $E_0$  is the normalized incident electric field magnitude,  $\phi_{EM}$  is the corresponding phase.  $\partial FoM / \partial T_M$  can be found by using the *chain rule* on  $\partial FoM / \partial E_M$ . Care must be taken because  $E_M$  is generally complex. One could take derivatives with respect to the real and imaginary parts of  $E_M$ . An equivalent and more convenient method is to take derivatives with respect to  $E_M$  and its complex conjugate as follows

$$\frac{\partial FoM}{\partial T_M(\mathbf{r}_M)} = \frac{\partial FoM}{\partial E_M(\mathbf{r}_M)} \frac{\partial E_M(\mathbf{r}_M)}{\partial T_M(\mathbf{r}_M)} + \frac{\partial FoM}{\partial E_M^*(\mathbf{r}_M)} \frac{\partial E_M^*(\mathbf{r}_M)}{\partial T_M(\mathbf{r}_M)} \quad (1.17)$$

where the asterisk \* denotes complex conjugation. Since  $FoM$  and  $T_M$  must be real, the two terms on the right hand side of Equation (1.17) are complex conjugates of each other. Thus, their imaginary parts cancel out, resulting in

$$\frac{\partial FoM}{\partial T_M(\mathbf{r}_M)} = 2Re \left[ \frac{\partial FoM}{\partial E_M(\mathbf{r}_M)} \frac{\partial E_M(\mathbf{r}_M)}{\partial T_M(\mathbf{r}_M)} \right] \quad (1.18)$$

Plugging Equation (1.16) into Equation (1.18), we obtain

$$\frac{\partial FoM}{\partial T_M(\mathbf{r}_M)} = 2Re \left\{ \frac{\partial FoM}{\partial E_M(\mathbf{r}_M)} E_0 \exp[i\phi_{EM}(\mathbf{r}_M)] \right\} \quad (1.19)$$

which translates from electric field gradient to the more operational mask transmission factor gradient.

For a spatially incoherent system modeled as a sum of coherent systems,  $\partial FoM / \partial T_M$  can be expressed as the total derivative with respect to the electric field of equally weighted angles of illumination.

$$\frac{\partial FoM}{\partial T_M(\mathbf{r}_M)} = \sum_n 2Re \left\{ \frac{\partial FoM}{\partial E_{Mn}(\mathbf{r}_M)} E_{0n} [i\phi_{EMn}(\mathbf{r}_M)] \right\} \quad (1.20)$$

where  $E_{Mn}$  is the mask plane electric field for the angle of illumination indexed by the integer  $n$ .

$\partial FoM / \partial T_M$  is the gradient with respect to the operational mask design parameters, and provides information about how the Figure-of-Merit changes as the transmission factor  $T_M$  changes at each point in space. Gradient descent, as in Newton's method for solving polynomial equations, operates by changing the mask transmission proportional to the rate of increase in the Figure-of-Merit:

$$\Delta T_M \propto \frac{\partial FoM}{\partial T_M} \quad (1.21)$$

where  $\Delta T_M$  is the change in  $T_M$  at a given iteration. As an optimum is approached, and the derivative approaches zero, the changes in  $T_M$  become smaller and smaller.

To model a binary amplitude mask, such as those used in EUV lithography, we constrain  $T_M$  to only take values of 0 or 1. Since the mask transmission is binary and does not take continuous values, the geometry update differs slightly from conventional gradient descent. Pixels in the mask are flipped only with the correct sign of  $\partial FoM / \partial T_M$ , and only when the gradient magnitude exceeds a threshold. The threshold is adjusted several times within each iteration to find the best improvement in the Figure-of-Merit. In this way, the iterative optimization procedure is well defined.

### 1.3.5 Figure-of-Merit

The Figure-of-Merit that we have preferred in these optimizations is the total error region area in which the printed pattern differs from the desired pattern. That area must be minimized. This Figure-of-Merit is illustrated by the grey region in Figure 3. Thus, the

error region is defined as

$$FoM = \int_W |P_d(\mathbf{r}_W) - p_a(E_W(\mathbf{r}_W))| d^2 r_W \quad (1.22)$$

where  $P_d$  and  $P_a$  are binary functions defining the desired and actual printed patterns, respectively. These are defined as

$$P_d(r_W) = \begin{cases} 0 & \mathbf{r}_W \in \text{desired dark region} \\ 1 & \mathbf{r}_W \in \text{desired bright region} \end{cases} \quad P_a(E_W(\mathbf{r}_W)) = \begin{cases} 0 & |E_W(\mathbf{r}_W)|^2 < I_{th} \\ 1 & |E_W(\mathbf{r}_W)|^2 \geq I_{th} \end{cases} \quad (1.23)$$

where  $I_{th}$  is the exposure threshold for electric field intensity. Anywhere the intensity is greater than  $I_{th}$ ,  $P_a$  is set to 1. Otherwise, its value is 0. Figure 3 shows an example of how the Figure-of-Merit is calculated.

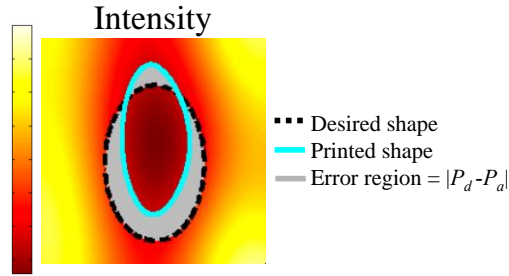


Figure 3 An example Figure-of-Merit calculation at the wafer plane. The color map shows electric field intensity. The desired pattern,  $P_d$ , is outlined by the black dashed line. The actual printed pattern,  $P_a$ , is outlined in cyan. The “error region”,  $|P_d - P_a|$ , is shown in gray. This error region is integrated to obtain the Figure-of-Merit.

The integrand of Equation (1.22),  $|P_d(\mathbf{r}_W) - P_a(E_W(\mathbf{r}_W))| \equiv f$ , must be differentiated to obtain the wafer plane gradient  $\partial f / \partial E_W$ . Unfortunately,  $P_a$  is not differentiable. Therefore, it is replaced by the continuous logistic function.

$$P_a(E_W(\mathbf{r}_W)) \approx \frac{1}{1 + \exp[-A(|E_W(\mathbf{r}_W)|^2 - I_{th})]} \equiv P'_a(E_W(\mathbf{r}_W)) \quad (1.24)$$

where  $A$  is a parameter defining the slope of the continuous differentiable function  $P'_a$ . To differentiate  $f$ , we replace the absolute magnitude with the square root of its square.

$$f = |P_d - P'_a| = [(P_d - P'_a)^2]^{\frac{1}{2}} \quad (1.25)$$

Differentiating, we obtain

$$\frac{\partial f}{\partial E_W} = \frac{1}{2} [(P_d - P'_a)]^{-\frac{1}{2}} 2(P_d - P'_a) \left( -\frac{\partial P'_a}{\partial E_W} \right) \quad (1.26)$$

$$= \frac{P'_a - P_d}{f} \left( \frac{\partial P'_a}{\partial E_W} \right) \quad (1.27)$$

We then differentiate  $P'_a$ ,

$$\frac{\partial P'_a}{\partial E_W} = \frac{1}{\{1+\exp[-A(|E_W|^2 - I_{th})]\}^2} \frac{\partial}{\partial E_W} \{\exp[-A(|E_W|^2 - I_{th})]\} \quad (1.28)$$

$$= -P'_a{}^2 \frac{\partial}{\partial E_W} \{\exp[-A(|E_W|^2 - I_{th})]\} \quad (1.29)$$

$$= AP'_a{}^2 E_W^* \exp[-A(|E_W|^2 - I_{th})] \quad (1.30)$$

where we used  $\partial|E_W|^2/\partial E_W = E_W^*$  [27]. Plugging Equation (1.30) into Equation (1.27), we obtain the wafer plane gradient

$$\frac{\partial f}{\partial E_W} = \frac{P'_a - P_d}{f} AP'_a{}^2 E_W^* \exp[A(|E_W|^2 - I_{th})] \quad (1.31)$$

We insert Equations. (1.31)&(1.15) into Equation (1.19), and then proceed with Equation (1.21) to complete one iteration.

For a spatially incoherent system modeled as a sum of coherent systems,  $|E_W|^2$  in Equation (1.23) is replaced by  $\sum_n |E_{Wn}|^2$ , where  $E_{Wn}$  is the wafer plane electric field resulting from one angle of illumination, indexed by the integer  $n$ . Differentiation with respect to  $E_{Wn}$  proceeds similarly to Equation (1.24)-(1.31).

## 1.4 Results

To test the method outlined in the previous sections, we consider a single lens lithography system as shown in Figure 2(b) that incorporates the aberrations to be expected in an equivalent single mirror EUV system as shown in Figure 2(a). The magnification is 0.25, as is the convention in photolithography. The lens/mirror diameter is  $D=30\text{cm}$ , with a numerical aperture at the wafer plane,  $NA_w=0.33$ . This leads to a mirror surface-to-wafer distance  $D/2\tan(\sin^{-1}NA_w)=S'=42.9082\text{ cm}$ . The mirror focusing equation,  $2/R=1/S'+1/S$  leads to a mirror surface-to-mask distance  $S=171.6328\text{ cm}$ , and a mirror radius of curvature  $R=68.6532\text{cm}$ . For these dimensions, a spherical mirror, relative to an ideal parabolic mirror, has aberrations amounting to  $>10000\lambda$  for  $\lambda=13.5\text{nm}$ . We assign 6 significant figures to the mirror radius of curvature owing to the need to specify the mirror surface within  $\sim 0.1\lambda$ , as is common in high precision optics. Indeed we have found that even  $\sim 0.1\lambda$  phase shift at the edge of the mirror produces  $\sim 10\%$  errors in the test pattern features, unless the mask is redesigned to account for the newly shifted mirror surface.

Six discrete plane waves are used for illumination. These points were chosen to give the illumination some of the characteristics of an extended dipole source. The illumination pattern used is shown in Figure 4. Our ILT mask solutions do correct aberrations very well, within the diffraction limit of the six selected illumination angles, but our solutions fail to accommodate the broad power from an extended incoherent source. We can model the incoherent source with more plane waves, but within the diffraction limit the number of plane waves would eventually equal the number of pixels. Each incident illumination angle imposes an additional constraint. For a totally incoherent source, the computation would not be manageable, nor would there be enough pixels in the mask to satisfy the multi-faceted constraints. This is discussed further in section 1.5. Thus, ILT for aberration correction is most suited to a partially coherent illumination source, like a laser.

Calculations of the basic Equation (1.11) are executed in MATLAB, using fast Fourier

transforms to compute the convolution with the point spread function. More mathematical details were discussed in section 2.3.1.

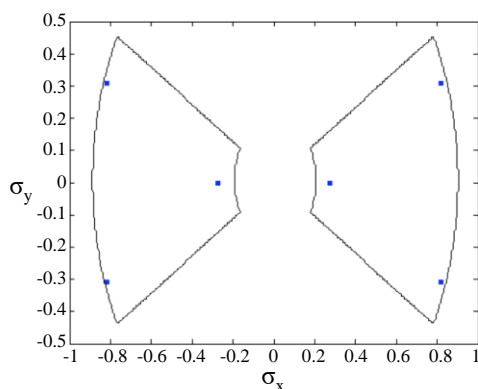


Figure 4 Illumination pattern.  $\sigma_x = \sin\theta_x/NA_W$  and  $\sigma_y = \sin\theta_y/NA_W$ . These six plane waves were chosen to give the illumination some of the characteristics of an extended dipole source, such as the one outlined in black. The four  $\sigma_x$  values are -0.8182, -0.2727, 0.2727, and 0.8182. The three  $\sigma_y$  values are -0.3099, 0, and 0.3099.

#### 1.4.1 Correcting Severe Spherical Aberration

We use a test pattern from an industry presentation [28], which is shown by the dashed lines in Figure 5(b). The pattern consists of six  $14\text{nm} \times 22\text{nm}$  features and one  $14\text{nm} \times 44\text{nm}$  feature. The features are placed  $50\text{nm}$  apart in the x-direction, and  $22\text{nm}$  apart in the y-direction. These dimensions should be compared with a diffraction limit  $\lambda/(4NA_W)=10\text{nm}$  for an EUV wavelength  $\lambda=13.5\text{nm}$ . The features are ellipsoidal to avoid sharp corners below the diffraction limit. The pattern in Figure 5(a) and Figure 6(a), is one unit cell of a periodic naïve mask, identical to the desired test pattern. The exposure threshold is taken to be half the clear field intensity.

For an un-aberrated case, the resulting wafer plane intensity and printed pattern are shown in Figure 5(b). For the spherically aberrated case, (corresponding to a  $30\text{cm}$  diameter focusing mirror) the wafer plane intensity and printed pattern are shown in Figure 6(b). In the un-aberrated case, Figure 5, all the features print. In Figure 6, the high spherical aberration produces 4 missing features and 3 unacceptable features. This spherical aberration relative to a perfect parabolic reflector has a peak value of  $>10000\lambda$  ( $>140\mu\text{m}$ ) based on Equation (1.8). The wafer is readjusted to the plane of best focus for this level of spherical aberration,  $\sim 2.6\text{mm}$  closer to the mirror than the best focus in the un-aberrated case.

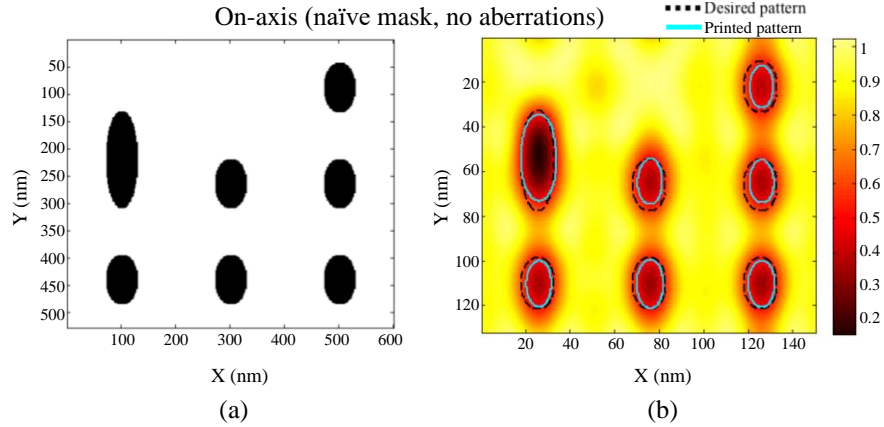


Figure 5 (a) mask and (b) wafer plane intensity (normalized to clear field) for an optical system with a naïve mask and no aberrations in the on-axis position. The pattern is periodic, with one unit cell shown. The NA of the system is 0.33, the demagnification is 4, and the wavelength is 13.5 nm.

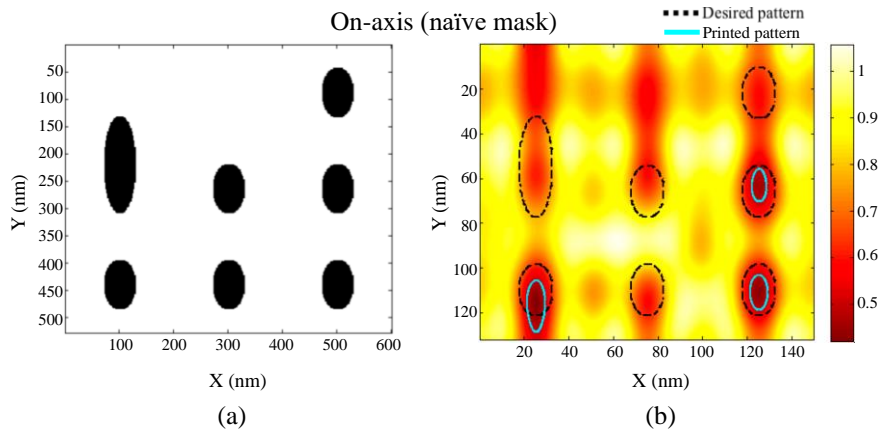


Figure 6 (a) mask and (b) wafer plane intensity (normalized to clear field) for an optical system with a naïve mask in the on-axis position. The pattern is periodic, with one unit cell shown. The NA of the system is 0.33, the demagnification is 4, and the wavelength is 13.5 nm. The mirror radius is 15 cm. The image was taken at the center of the field. This naïve mask is used as the starting geometry for the optimization.

Using the test pattern in Figure 6(a) as a starting point, we used our adjoint optimizer, Equation (1.21), to optimize the mask. The pixel size for the simulation during optimization is 0.25 nm at the wafer plane and 1nm at the mask plane. After optimization, the mask solution is tested with a smaller pixel size=0.16nm at the mask plane, for validation. This change in pixel size is done to ensure the critical dimensions of the final shape are computed to within less than 1% accuracy during final analysis. This accuracy is not critically needed during optimization, but is important in validation. The optimized mask appearance is shown in Figure 7(a). In the intensity profile of Figure 7(b) all critical dimensions were achieved to within 5%. The optimization took 148 iterations to converge.

Roughly 3 pixel-flip thresholds were compared per iteration, as discussed at the end of section 1.3.4. Additionally, a radius of curvature constraint  $<12\text{nm}$  was imposed on the mask at each iteration. This radius of curvature constraint is applied by morphological opening as described in [29].

A coarser, pixelated, version of the optimized mask in Figure 7 is shown in Figure 8, with the mask constructed from  $14\text{nm} \times 15\text{nm}$  rectangles to make the mask conform to Manhattan geometry. After pixelation, all critical dimensions are still achieved to within 8%. This demonstrates the robustness of the mask design.

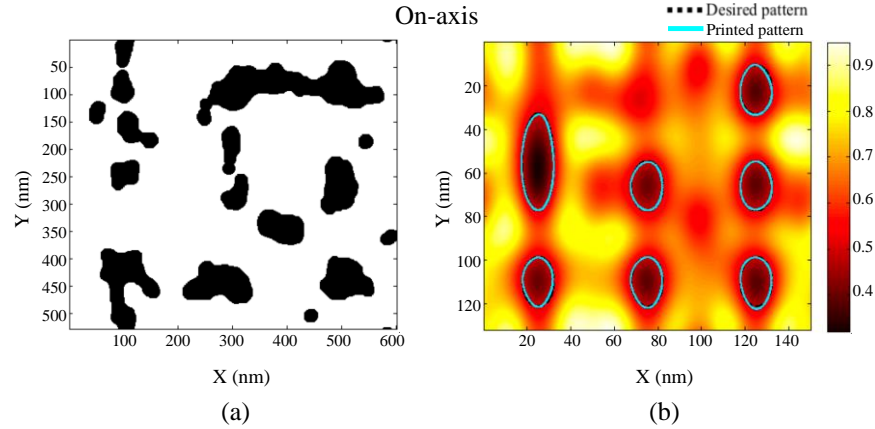


Figure 7 (a) Mask and (b) wafer plane intensity (normalized to clear field) for an optical system with an optimized mask. The simulation conditions are the same as in Figure 6. With this optimized mask, all critical dimensions are within 5% of their target.

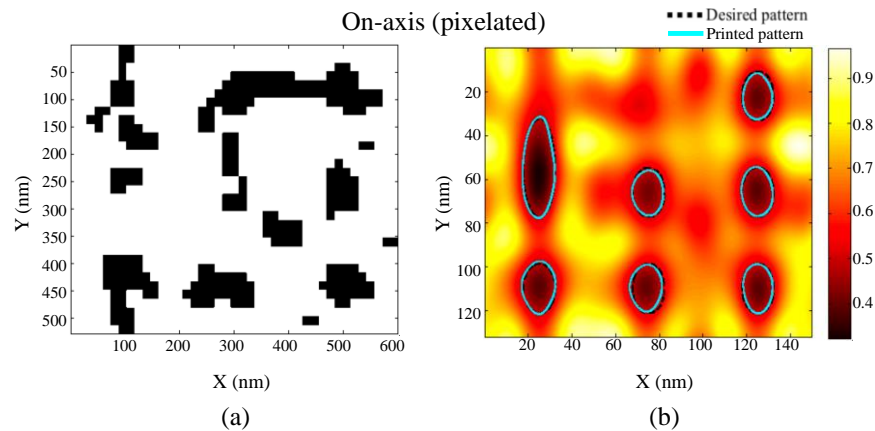


Figure 8 The same optical system as in Figure 7, with the mask pixelated. The pixels are  $14\text{nm} \times 15\text{nm}$ . All critical dimensions are within 8% of their target.

### 1.4.2 Depth-of-Focus Optimization

We have also performed mask optimization as a function of focal depth. To do this, we began with the optimal mask at focus, and then optimized the Figure-of-Merit at 4 planes:  $-50\text{nm}$ ,  $-30\text{nm}$ ,  $-10\text{nm}$ , and  $+10\text{nm}$  relative to the initial optimal plane, to investigate a  $60\text{nm}$  depth of focus. The Figure-of-Merit is the sum of area errors, as in

Equation (1.22), summed over all 4 image planes. Figure 9 shows the mask and wafer field at nominal focus resulting from this optimization. Roughly 5 pixel-flip thresholds were compared per iteration, as discussed at the end of section 1.3.4. This optimization required 339 iterations.

Figure 10(a) shows a Bossung plot for the worst performing feature for the mask optimized at focus, and Figure 10(b) for the mask simultaneously optimized at the four different planes -50nm to +10nm. The sharp jumps seen in the plots correspond to changes in the location of the worst performing feature. For the mask optimized through focus, all critical dimensions remain within 11% for the full 60nm of defocus at nominal dose. The dose sensitivity, not optimized here, could be expected to improve if optimized.

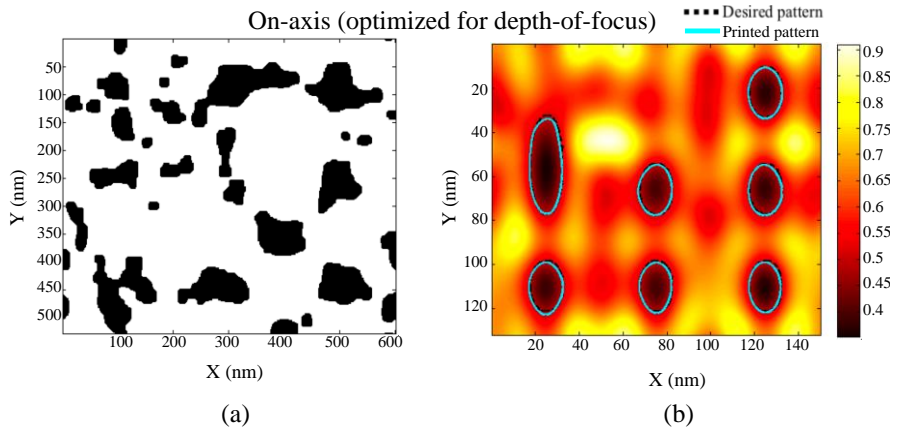


Figure 9 (a) Mask and (b) wafer plane intensity (normalized to clear field) for an optical system with a mask optimized to perform through 60nm of defocus. The simulation conditions are the same as in Figure 5. With this mask, all critical dimensions are within 7% of their target at focus, and remain within 11% through 60nm of defocus.

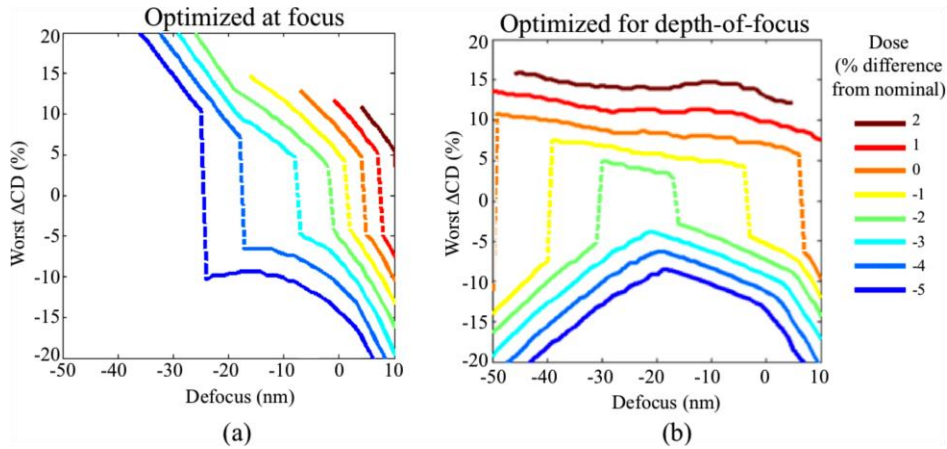


Figure 10 Bossung plots for the worst performing feature for the masks optimized (a) at focus, and (b) for depth-of-focus. For the mask optimized through focus, all critical dimensions remain within 11% of their targets for 60nm of defocus at nominal dose. The sharp jumps seen in the plots correspond to changes in the location of the worst performing feature.

### 1.4.3 Off-axis Aberration Correction

We have considered severe spherical aberrations, combined with a depth of field requirement. Now we consider off-axis imaging, which includes, spherical aberration, coma, and astigmatism, all severe owing to the use of an uncorrected spherical optic. The additional aberrations change the point spread function used in simulation according to Equation (1.2), (1.3), and (1.8) in section 1.3.1. The off-axis points are in a 33mm  $\times$  26mm wafer and are shown in Figure 11. The mid-field point 6.5mm off-center is  $\sim 0.9^\circ$  off-axis, and the field edge-point 13mm off-center is  $\sim 1.8^\circ$  off-axis. The mid-field point experiences  $>4000\lambda$  of coma and  $>230\lambda$  of astigmatism in addition to the spherical aberration present in the on-axis case. The field edge point experiences  $>9000\lambda$  of coma, and  $>900\lambda$  of astigmatism. For simplicity we don't account for aberration variation within the 150nm  $\times$  132nm test pattern unit cell. This variation is relatively small, but must be taken into account in an industrial application.

The results for the mid-field optimization are shown in Figure 12. The optimized mask for the on-axis case, Figure 7(a) was used as the starting point for this optimization. After the final iteration, the critical dimensions are within 2% of the desired target. During optimization, the simulation pixel size was 2nm at the mask plane. As before, the pixel size was reduced to 0.16nm at the mask plane to accurately validate the critical dimensions after the last iteration. This optimization took 313 iterations with roughly 3 pixel-flip thresholds tested per iteration, as discussed at the end of section 1.3.4.

The results for the field edge case are shown in Figure 13. The optimized mask for the mid-field case was used as the starting mask for this optimization. After the final iteration, all critical dimensions are within 3% of their desired target. During optimization, the simulation pixel size was 2nm at the mask plane. For validation after the last iteration, the pixel size was reduced to 0.16nm at the mask plane. This optimization took 185 iterations with roughly 3 pixel-flip thresholds tested per iteration, as discussed at the end of section 1.3.4.

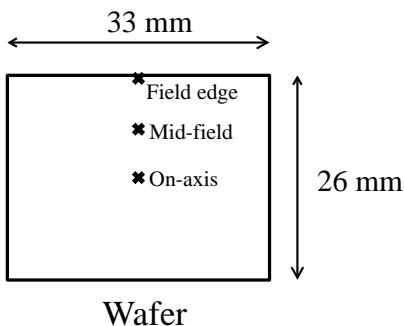


Figure 11 A diagram showing the three points on the wafer we designed masks for. The wafer was assumed to be 33 by 26 mm. The mid-field point is displaced 6.5 mm from the optical axis and has  $>4000$  wavelengths of coma and  $>230$  wavelengths of astigmatism (peak value, using the convention in Equation (1.8) ). The field edge point is displaced 1.3 mm and has  $>9000$  wavelengths of coma, and  $>900$  wavelengths of astigmatism.

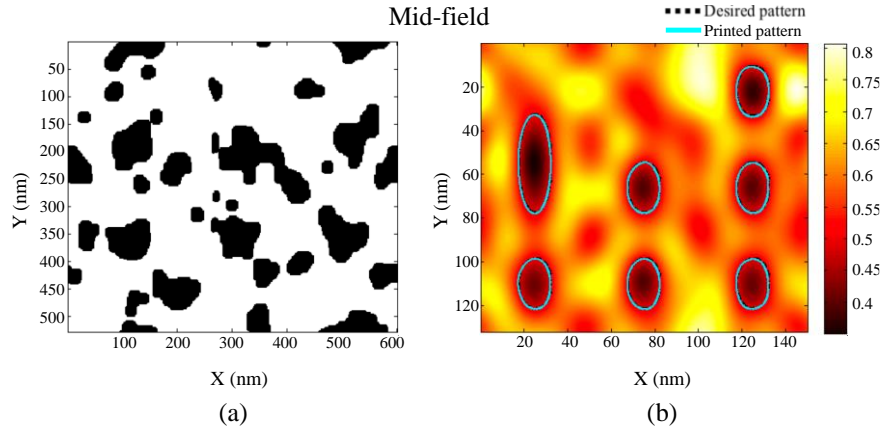


Figure 12 (a) Mask and (b) wafer plane intensity (normalized to clear field) after optimization for the mid-field location 6.5mm off-axis. The mask resulting from the on-axis optimization was used as the starting mask for this optimization. All critical dimensions are within 2% of their target.

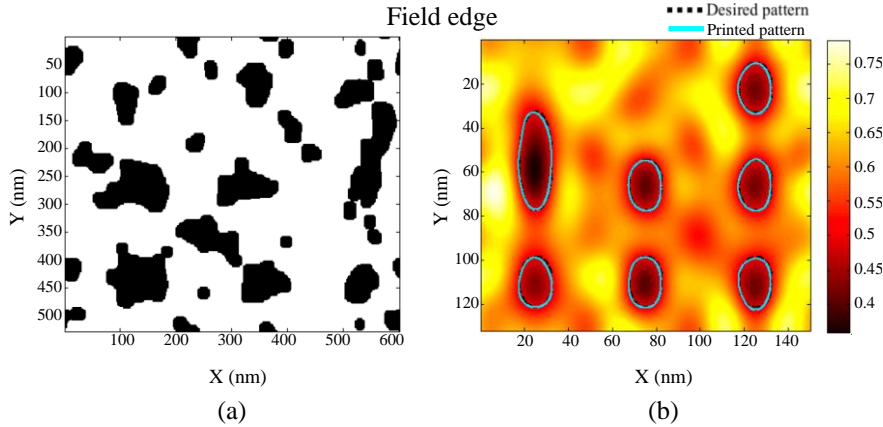


Figure 13 (a) Mask and (b) wafer plane intensity (normalized to clear field) after optimization for the field edge location 13mm off-axis. The mask resulting from the mid-field optimization was used as the starting mask for this optimization. All critical dimensions are within 3% of their target.

A comparison of Figure 7(a), on-axis, Figure 12(a), 6.5mm off-axis, and Figure 13(a), 13mm off-axis, show completely different mask solutions, even though the test pattern was identical. The mask solution is sensitive to the exact level of aberrations. A mask solution at the center of a chip would be different from a mask solution at the edge of a chip. Even with a repeating pattern as in a DRAM chip, the mask would be aperiodic, and computationally intensive to design.

We have considered spherical aberration, and off-axis aberrations coma and astigmatism. Additional aberrations can be trivially included in the current model by adding more terms to the phase shift at the mirror; therefore changing the point spread function. Additionally, in an industrial application, the Figure-of-Merit should include tolerances toward exposure dose and errors in photomask fabrication. Since off-axis aberrations vary across the chip-field, a global optimization across the whole chip would be required.

In addition, electromagnetic edge effects in the mask, and angle-dependent mirror reflectivity, must also be accounted for in the simulation. This does not pose problems to the optimization method, since our implementation of the adjoint method can wrap around any Maxwell solver.

## 1.5 Angular Sensitivity Analysis

Under severe aberrations, the printed pattern on the wafer for a coherent source becomes sensitive to small changes in the angle of illumination. This has implications for an incoherent source with a continuous spread of illumination angles. Since the incoherent source is represented as the sum of coherent sources, the angular precision of a coherent source determines how many coherent plane waves will need to be simulated to accurately represent the incoherent source. If this number is sufficiently large, there will not be enough design degrees of freedom to successfully design the mask.

The reason for the angular sensitivity from aberrations is illustrated in Figure 14. Figure 14 depicts a coherent system with one lens for the purposes of illustration. When the angle is changed by  $\Delta\theta$ , the position of a diffracted order on the lens shifts by  $\Delta r_L$ , where  $r_L$  is the lateral spatial coordinate on the lens in the direction of the angle change. This changes the aberration phase shift seen by the diffracted order by  $\Delta\delta$ . For different diffracted orders,  $\Delta\delta$  will be different. This results in a different complex field on the lens, and hence a different field on the wafer.

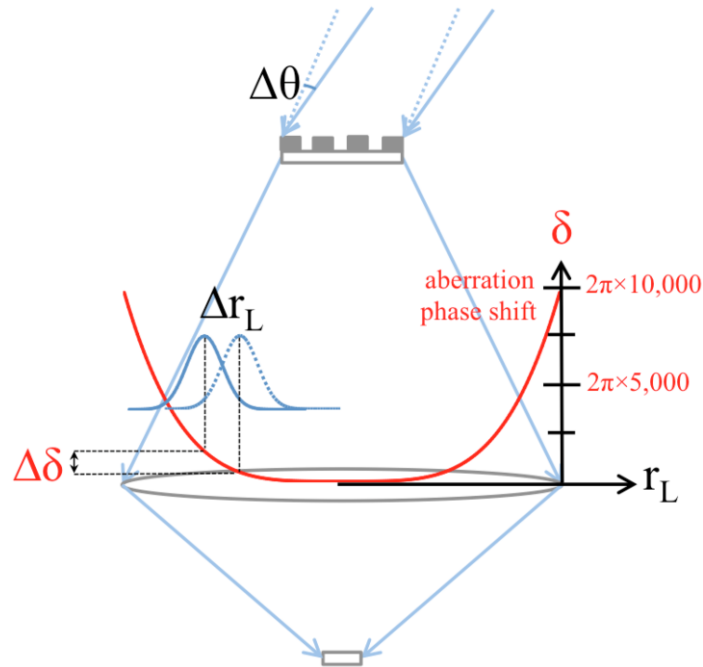


Figure 14 A diagram showing how the angular sensitivity,  $\Delta\theta$  of an illumination plane wave depends upon the magnitude of aberration phase shift on the lens of an optical system.

To calculate the tolerable  $\Delta\theta$ , we will assume a tolerable  $\Delta\delta$  at the edge of the lens of  $0.1\lambda$ . This is the  $\Delta\delta$  that is likely to cause  $\sim 10\%$  change in critical dimension in the wafer image. We note the relationship between  $\Delta\theta$  and  $\Delta\delta$

$$\Delta\delta = \frac{\partial\delta}{\partial r_L} \Delta r_L = \frac{\partial\delta}{\partial r_L} S \Delta\theta, \quad (1.32)$$

where  $S$  is the distance between the mask and the lens. From here, we note that if there is significant overlap between a diffracted order before and after an angle shift (the solid and dashed blue lines above the lens in Figure 14), the total electric field is affected less by the angle shift. To accommodate this, we make a modification to Equation (1.32) if the angle shift  $\Delta\theta$  is less than  $\theta_w = \lambda/\Lambda$ , the angular width of one diffracted order (where  $\Lambda$  is the width of the mask).

$$\Delta\delta_{eff} = \begin{cases} \frac{\partial\delta}{\partial r_L} S \Delta\theta & \Delta\theta > \theta_w \\ \frac{\partial\delta}{\partial r_L} S \Delta\theta \frac{\Delta\theta}{\theta_w} & \Delta\theta < \theta_w \end{cases}, \quad (1.33)$$

The second case in Equation (1.33) multiplies Equation (1.32) by the fraction  $\Delta\theta/\theta_w$  to give an estimate of the effective  $\Delta\delta$  from  $\Delta\theta$ .

We will assume spherical aberration, for which  $\delta(r_L)$  has the form  $\delta(r_L) = ar_L^4$ . Plugging in the numbers  $S=1.71\text{m}$ ,  $\Delta\delta_{eff}=0.1\lambda$ ,  $\lambda=13.5\text{nm}$ ,  $\delta(r_{L,max})=10,000\lambda$ ,  $r_{L,max}=15\text{cm}$ , and  $\Lambda=104\text{mm}$  into Equation (1.33); we obtain  $\Delta\theta=10^{-5^\circ}$ . With an illumination cone with a maximum angle of  $5^\circ$ , this means we would need to optimize for  $\pi(5^\circ/10^{-5^\circ})=8 \times 10^{11}$  separate coherent sources. This is much larger than the number of degrees of freedom in the mask ( $\sim 3 \times 10^5$ ). This implies that our method cannot be used with a coherent source and a large mask. Nonetheless, it would work well with a partially coherent source such as a laser. Thus, such a source for EUV warrants more scientific effort.

## 1.6 Conclusion

We have shown that, under a partially coherent source, like a laser, Inverse Lithography Technology can allow EUV Lithography to proceed in spite of severe aberrations, (as would be produced by a single-mirror imaging system). By reducing from 6 mirrors to 1 mirror, the power wasted by the projection optics would be reduced by  $\sim 7\times$ , owing to the diminished mirror losses with fewer mirrors. Since ILT is needed for mask optimization, the strategy of also using it for aberration correction seems well warranted. We have successfully designed photomasks to print test patterns in the presence of severe spherical aberration and including off-axis coma and astigmatism, and the requirement for 60nm depth of focus.

If we force current incoherent EUV sources to produce a six-beam illumination pattern as in Figure 4, the throughput would be very limited. Thus, a partially coherent EUV source, like a laser should warrant more scientific and technological effort.

## 2 Hybrid Solar Photovoltaic and Solar Thermal Collection System

### 2.1 Opportunities enabled by highly reflective, high efficiency photovoltaics

Improvements in light management in photovoltaics have recently enabled solar cells with efficiencies that approach ever closer to the Shockley-Queisser limit. In particular, Alta Devices have achieved a record efficiency of 28.8% with single-junction gallium arsenide solar cells under 1-sun illumination [30]. This was achieved, in part, due to improvements in the back reflectivity of the cells.

High back reflectivity benefits photovoltaic cells by increasing the light concentration inside the cell. The increase in light concentration corresponds to an increase in carrier density. A higher carrier density has more free energy, and therefore increases the voltage of the photovoltaic cell. The increase in light concentration at open circuit condition, resulting from a back mirror, is illustrated in Figure 15 and Figure 16.

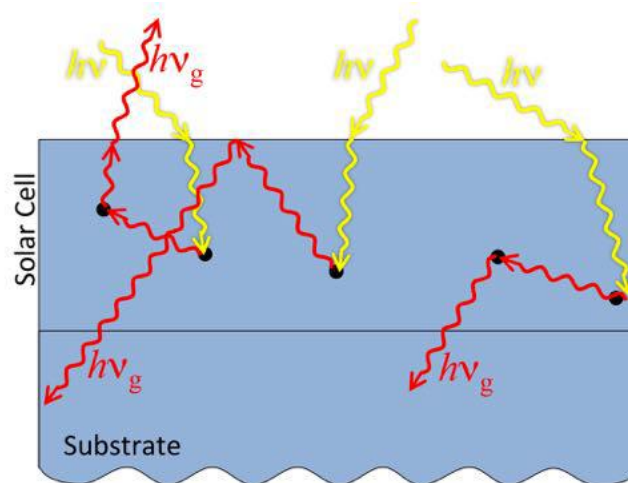


Figure 15 Diagram of a solar cell at open circuit on an index-matched semiconductor substrate. Incident photons, shown in yellow, refract toward the normal upon entering the semiconductor due to the index mismatch with air. The incident photons are absorbed and re-emitted. The re-emitted photons have an energy equal to the bandgap energy of the semiconductor, and are shown in red. The re-emitted photons tend to escape into the substrate before they can build up a high light intensity.

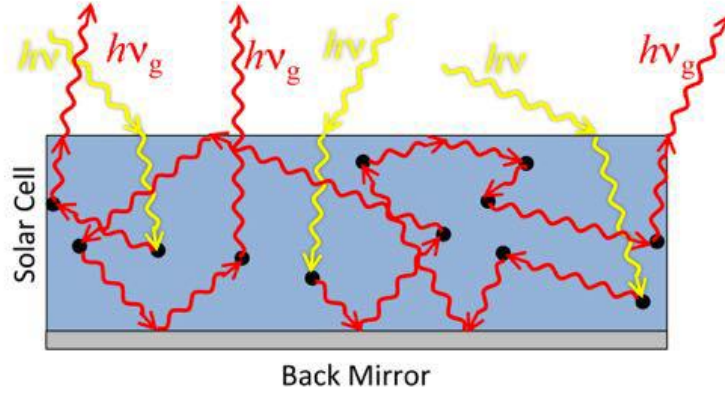


Figure 16 Diagram of a solar cell at open circuit with a perfectly reflecting back mirror. In this case, the re-emitted photons are absorbed and re-emitted many times. This causes the light intensity to build up inside the cell. The re-emitted photons eventually escape out the front of the cell.

The increase in light concentration from a back mirror is due to reflections of re-emitted photons inside the cell. Conventional III-V solar cells are grown in a lattice-matched substrate. Such a cell under open circuit condition is depicted in Figure 15. In this case, many of the re-emitted photons are lost inside the substrate. In the case of a cell with a back mirror, shown in Figure 16, the re-emitted photons are reflected back into the cell, building up the light intensity inside the cell. They may be reflected many times due to reflection at the interface between the semiconductor and air at the front surface. Thus, the intensity of light re-emitted out the front surface of the photovoltaic cell at open circuit condition is a measure of the free energy, and hence the voltage of the cell. The fraction of light absorbed that is eventually re-emitted out the front surface is referred to as the external luminescence efficiency of the cell. The remainder of this section will mathematically explain how external luminescence efficiency determines open circuit voltage.

We will analyze an ideal single bandgap photovoltaic cell, as described by Shockley and Quisser in [31]. This analysis is also detailed in [32]. This ideal cell has step function absorption, a perfect antireflection coating, and infinite carrier mobility.

Consider the cell when it is in the dark, at thermal equilibrium with its surroundings. It will absorb black body radiation from the surroundings. This is given by

$$b(E) = \frac{2\pi E^2}{c^2 h^3 \left( \exp\left(\frac{E}{k_B T}\right) - 1 \right)} \quad (2.1)$$

where the units of  $b$  are [photons/(time  $\times$  area  $\times$  energy  $\times$  steradian)].  $E$  is the photon energy,  $h$  is Planck's constant,  $c$  is the speed of light, and  $k_B T$  is the thermal energy.

The photon flux into the front of the photovoltaic cell is given by

$$L_{bb} = 2\pi \int_0^\infty \int_0^{\frac{\pi}{2}} A(E)b(E)\sin\theta\cos\theta d\theta dE \quad (2.2)$$

Where  $\theta$  is the angle from normal to the cell, and  $A(E)$  is the step function absorptivity for the bandgap of the semiconductor. In thermal equilibrium,  $L_{bb}$  is the photon flux out the front surface of the cell as well.

When the sun illuminates the cell, it moves into quasi-equilibrium. In quasi-equilibrium, The cell remains at the same temperature, and the photon flux out the front of the cell is still given by Eq (2.2). The flux into the cell is given by

$$S(E) = \frac{2\pi E^2}{c^2 h^3 \left( \exp\left(\frac{E}{k_B T_s}\right) - 1 \right)} \quad (2.3)$$

where  $T_s$  is the temperature of the sun.

Under the quasi-Equilibrium condition, the cell has a chemical potential of  $qV$ , where  $q$  is the electron charge, and  $V$  is the voltage. The separation between the quasi-Fermi levels is equal to  $qV$ . Under illumination, the photon flux out the front surface is given by

$$L_{ext}(V) = \exp\left(\frac{qV}{k_B T}\right) L_{bb} = \exp\left(\frac{qV}{k_B T}\right) 2\pi \int_{E_g}^\infty \int_0^{\frac{\pi}{2}} b(E)\sin\theta\cos\theta d\theta dE. \quad (2.4)$$

The external luminescence efficiency,  $\eta_{ext}$  is defined as the ratio of the rate of radiative flux out the top,  $L_{ext}$ , to the total radiative flux, which includes radiative flux out the bottom of the cell and non-radiative recombination in the cell.

$$\eta_{ext} = \frac{L_{ext}}{L_{total}} \quad (2.5)$$

The absorption of photons from the sun is  $\int_0^\infty A(E)S(E)dE$ . The current of the solar cell is given by the absorption of photons from the sun minus the emission of photons out of the cell. Rearranging Equation (2.5), we obtain  $L_{total}=L_{ext}/\eta_{ext}$ . Thus, the J-V characteristic of the photovoltaic cell is given by

$$J(V) = \int_{E_g}^\infty S(E)dE - L_{total} = \int_{E_g}^\infty S(E)dE - \frac{\pi}{\eta_{ext}} \exp\left(\frac{qV}{k_B T}\right) \int_{E_g}^\infty b(E)dE \quad (2.6)$$

where  $J$  is the current density and  $V$  is the voltage. Equation (2.6) shows how the external luminescence efficiency impacts the J-V characteristics of a photovoltaic cell, but this equation can be rearranged to show explicitly how the luminescence efficiency influences the open circuit voltage. The open circuit voltage is the primary parameter influenced by the luminescence efficiency. Setting  $J=0$ , and solving for  $V$  in Equation (2.6), we obtain

$$V_{OC} = \frac{k_B T}{q} \ln\left(\frac{\int_{E_g}^\infty S(E)dE}{\pi \int_{E_g}^\infty b(E)dE}\right) - \frac{k_B T}{q} \ln\left(\frac{1}{\eta_{ext}}\right). \quad (2.7)$$

In Equation (2.7), it can be seen that a value of  $\eta_{ext}$  less than one results in a penalty to  $V_{OC}$ , as per the second term in the right hand side of the equation. Thus, Equation (2.7) can be rewritten as

$$qV_{OC} = qV_{OC,ideal} - K_B T \ln\left(\frac{1}{\eta_{ext}}\right). \quad (2.8)$$

$$qV_{OC} = E_g - q\Delta V_{OC,ideal} - K_B T \ln\left(\frac{1}{\eta_{ext}}\right). \quad (2.9)$$

Note the similarity of Equation (2.9) to the general formula for the Helmholtz free energy

$$F = U - TS \quad (2.10)$$

where  $F$  is the free energy,  $U$  is the internal energy, and  $S$  is the entropy loss. The energy available from a carrier to do work at open circuit condition is given by  $qV_{OC}$ . A carrier generated from an absorbed photon starts out with the bandgap energy,  $E_g$ . The remaining terms on the right hand side of Equation (2.9) are entropic losses. A more detailed description of the entropic losses in a photovoltaic cell is available in [18]. This analogy between Equation (2.9) and Equation (2.10) helps illustrate the claim that a photovoltaic cell with a high external luminescence efficiency has a higher free energy, and hence a higher open circuit voltage.

Recall that an imperfect external luminescence efficiency is caused by two different factors: nonradiative recombination of carriers, and photons lost out the back of the photovoltaic cell. Photons are lost out the back if there is no back mirror, or an imperfect back mirror. Therefore, a highly reflective back mirror is a critical part of a highly efficient photovoltaic cell. Since record-breaking solar cells already have this high reflectivity, it is possible to conceive of applications in which this reflectivity is leveraged for other purposes as well. In the remainder of this chapter, we will explore one such application, the hybrid solar photovoltaic and solar thermal collector.

## 2.2 Background for Hybrid Photovoltaic/Thermal Systems

High utilization of solar energy, renewable, clean, and abundant source, is an important component for future energy needs that will ensure energy independence and low environmental impact [33]. Solar energy is available at no cost, but efficient collection, storage, and use of this energy in an economical way remains a challenge. Hybrid photovoltaic/thermal systems use a combination of photovoltaic devices and solar thermal collectors to produce both heat and electricity. Incident photon energy on a photovoltaic device that does not produce electricity builds up as heat. Rather than wasting this energy, hybrid systems collect it using a heat transfer fluid. The concept of hybrid photovoltaic/thermal systems was developed in the 1970s [34] and since then a significant amount of research and development work on hybrid photovoltaic/thermal technology has been done as extensively reviewed in Refs. [35]–[45]. Hybrid photovoltaic/thermal systems differ in fluid temperature, heat transfer fluid type, concentration ratio, photovoltaic cell type, thermal efficiency, and electrical efficiency. The most common heat transfer fluids used in hybrid photovoltaic/thermal technologies are air [35], [42], [46] or water [44], [47], [48]. While air systems are generally simpler, water based hybrid photovoltaic/thermal systems are more efficient due to the higher heat capacity of water. Both of these designs are limited to relatively low temperatures applications. The performance of a hybrid photovoltaic/thermal system depends on the photovoltaic device as well, with most systems using mono-crystalline (Mono-Si), multicrystalline (Multi-Si), or thin film amorphous silicon (a-Si) [49], [50]. Crystalline silicon solar cell types are

more efficient, but are affected much more negatively at higher working temperatures compared to the thin film photovoltaics [51]–[53]. Most studies of hybrid photovoltaic/thermal collectors deal with flat plate collectors [39], [44], or low concentration nonimaging systems [54], [55]. In Ref. [54] the authors reported on a water-cooled hybrid photovoltaic/thermal system with a 4× concentration ratio using compound parabolic concentrators with a maximum fluid temperature of 65°C. In Ref. [55], the concentrator was designed using a Fresnel lens and flat mirrors to get a uniformly concentrated irradiation on the solar cells. To date there has been little to no work in the field of medium to high concentration photovoltaic/thermal collectors operating at high temperature due to increased system complexity added by cooling mechanisms, trackers, and solar cell performance at elevated temperatures. The combined heat and power solar system (CHAPS) [49] consists of glass-on-metal mirrors that focus light onto Mono-Si solar cells with a geometric concentration ratio of 37×. It is water cooled and reaches an outlet temperature of 80°C. The use of high efficiency thin films solar cells such as Gallium Arsenide (GaAs) in hybrid photovoltaic/thermal systems is rarely investigated in the literature, despite the fact that GaAs cells have better efficiencies and temperature coefficients than silicon solar cells [56]. The purpose of this study is to design, simulate, and test a novel parabolic trough hybrid photovoltaic/thermal solar collector capable of producing electricity directly and high temperature thermal energy to be stored for on-demand electricity production. Using nonimaging optics the receiver is transformed into a spectrum-splitting device. The proposed system uses world record single-junction GaAs solar cells with high back reflectivity, allowing them to produce electricity from high energy photons while reflecting lower energy photons to a thermal absorber. This unique double stage concentrator design achieves a concentration ratio ~60×, which is significantly higher than conventional hybrid photovoltaic/thermal systems. This helps achieve high temperatures under partial utilization of the solar spectrum and maximizes the exergy efficiency output of the system.

### 2.3 Experimental Hybrid Solar Photovoltaic/Thermal System

A schematic of our implementation of the hybrid solar photovoltaic/thermal system is depicted in Figure 17. Direct normal irradiance from the sun is collected by the primary reflector, a parabolic concentrating mirror. This light is concentrated onto a secondary reflector composed of gallium arsenide (GaAs) photovoltaic cells. The photovoltaic cells absorb the portion of the spectrum above their bandgap, and reflect the remaining below-bandgap light. These cells are arranged in a parabolic shape around a high temperature absorber, so that the reflected below-bandgap light is concentrated on the absorber. The absorber contains a heat transfer fluid that is continuously pumped through it to transfer the thermal energy to where it can be harvested. The work described in this section was done in collaboration with the Winston group of UC Merced, and was previously presented in refs. [57], [58].

The primary concentrator has an area of 5m<sup>2</sup>. The secondary concentrator (curved reflector in Figure 17) has an area of 0.111m<sup>2</sup>. The light concentration onto the secondary concentrator can be found with the ratio of these two areas.  $C_1=5\text{m}^2/0.111\text{m}^2=45\times$ . The high temperature absorber that receives the radiation has an area of 0.0839m<sup>2</sup>. The

concentration ratio in the second stage is  $C_2=0.111\text{m}^2/0.0839\text{m}^2=1.325\times$ . The total concentration is  $C_1*C_2=59.6\times$ .

Several system components are depicted in Figure 18. Figure 18(a) shows a photograph of the primary concentrator with structural supports for the secondary concentrator and absorber. Figure 18(b) shows a GaAs photovoltaic cell used in the secondary concentrator. Figure 18(c) shows the secondary concentrator and absorber inside evacuated glass tube, covered in GaAs photovoltaic cells.

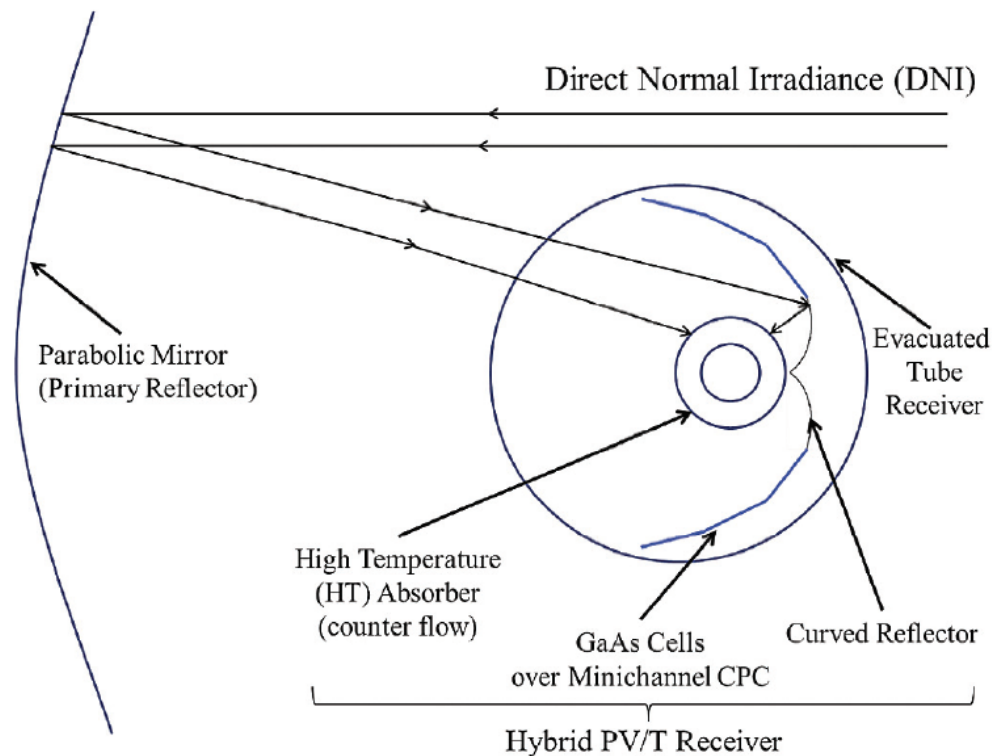
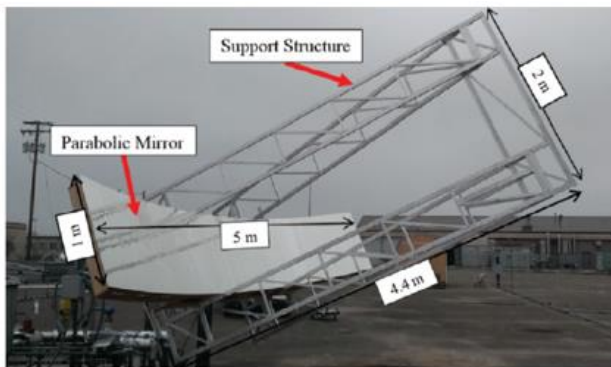
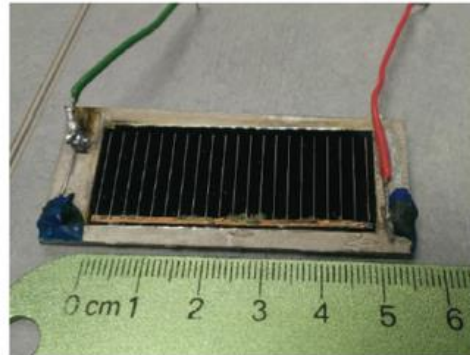


Figure 17 Hybrid solar photovoltaic/thermal system. Direct normal irradiance from the sun is collected by the primary reflector, a parabolic concentrating mirror. This light is concentrated onto a secondary reflector composed of gallium arsenide (GaAs) photovoltaic cells. The photovoltaic cells absorb the portion of the spectrum above their bandgap, and reflect the remaining below-bandgap light. These cells are arranged in a parabolic shape around a high temperature absorber, so that the reflected below-bandgap light is concentrated on the absorber. The absorber contains a heat transfer fluid that is continuously pumped through it to transfer the thermal energy to where it can be harvested.

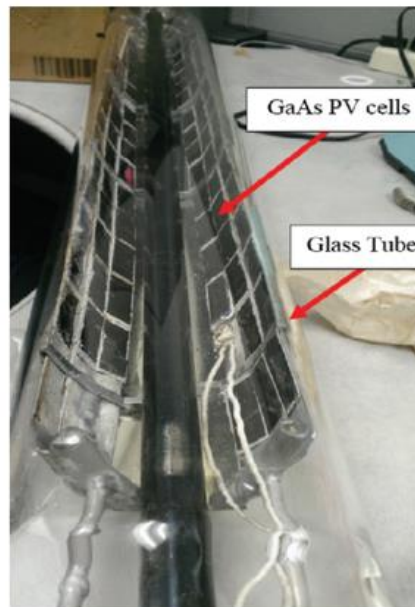
The high temperature stream of heat transfer fluid (Duratherm 600) in the high temperature absorber is designed to heat up to a temperature of  $500^{\circ}\text{C}$ . The absorber is covered in a coating from Himin Solar Co. with a tailored emissivity so that it absorbs heavily from the solar spectrum, but has minimal emission for the  $500^{\circ}\text{C}$  blackbody spectrum. This is illustrated in Figure 19.



(a)



(b)



(c)

Figure 18 System components. (a) photograph of primary concentrator with structural supports for the secondary concentrator and absorber. (b) GaAs photovoltaic cell from Alta Devices. (c) Secondary concentrator and absorber inside evacuated glass tube, covered in GaAs photovoltaic cells.

The heat collected from the high temperature absorber channel is given by

$$Q_{high T} = \dot{m}_{high T} c_p (T_{out,high T} - T_{in,high T}). \quad (2.11)$$

The cooling channels behind the GaAs photovoltaic cells constitute the low temperature stream. They contain heat transfer fluid as well, and is designed to heat up to a temperature of 200°C. The heat collected is similarly given by

$$Q_{low T} = \dot{m}_{low T} c_p (T_{out,low T} - T_{in,low T}). \quad (2.12)$$

The total useable energy from the system is referred to as exergy. The total exergy efficiency of the system is given by

$$\eta_{exergy} = \frac{Q_{low T} \eta_{Carnot,low T} + Q_{high T} \eta_{Carnot,high T} + E_{electrical}}{G}, \quad (2.13)$$

where G is the total power incident on the primary reflector. Here,  $\eta_{Carnot}$  is the Carnot efficiency of a heat engine producing work from the harvested heat. This represents the maximum possible. It is given by

$$\eta_{Carnot} = 1 - \frac{T_{cold}}{T_{hot}}. \quad (2.14)$$

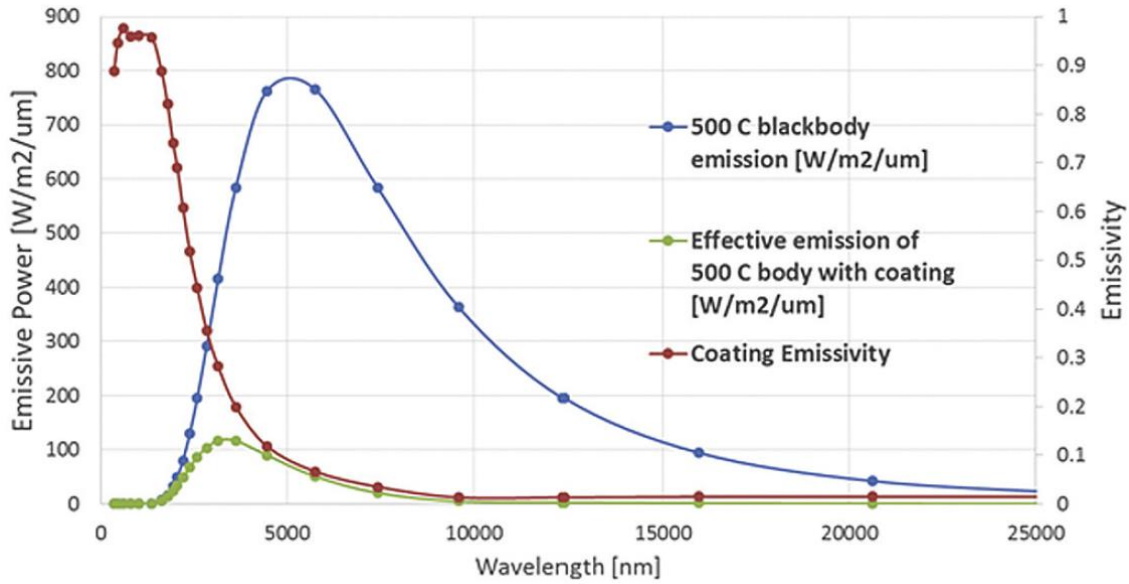


Figure 19 Emissive power and emissivity of the high temperature absorber. The red curve shows the emissivity/absorptivity of the absorber (data from Himin Solar Co.). The absorber is tailored to be high in the low wavelength (high photon energy) region to maximize absorption from the solar spectrum. The absorber is also tailored to have a low emissivity in the long wavelength (low photon energy) portion of the spectrum, that overlaps with most of the blackbody spectrum for a temperature of 500°C. The blue curve shows this blackbody spectrum. A low emissivity in this region prevents unwanted energy loss from the absorber via radiation. The effective emission from the high temperature absorber is shown in the green curve.

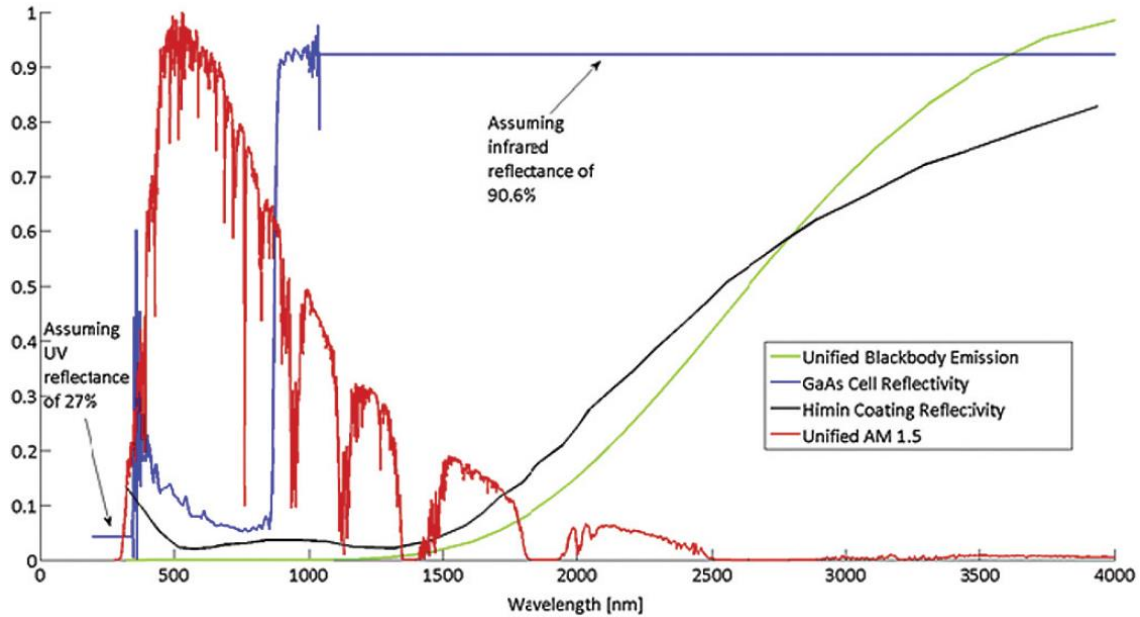


Figure 20 Photovoltaic cell and high temperature coating reflectivity versus blackbody emission and AM 1.5 solar spectrum. The red curve depicts the AM 1.5 spectrum, representing solar radiation. The blue curve depicts the reflectivity of the GaAs photovoltaic cells from Alta Devices used in the system, with constant extrapolations for the infrared and ultraviolet regions. The black curve depicts the reflectivity of the coating from Himin Solar Co. used on the high temperature absorber. The green curve depicts the black body emission from the high temperature absorber. All radiation spectra shown are normalized so that the maximum value is equal to 1.

## 2.4 Modeling Results

An optical model of the system was developed and analyzed using LightTools illumination design software. This is discussed in greater detail in ref. [58]. The optical model includes the spectral reflectivity of the different components. The reflectivity used for the GaAs photovoltaic cells is depicted by the blue curve in Figure 20. The high and low ends of the spectrum are extrapolated beyond the measured portion of the spectrum, and assumed to be constant values in this region. Optical modelling of the system was performed with uniformly distributed rays within a  $0.8^\circ$  cone. Of the total incoming light, 82% is incident on the aperture of the second concentrator. Of the incoming direct normal irradiation, 47% is captured in the absorber, and 26% is captured in the photovoltaic cells.

The thermal performance of the system was modelled with finite element analysis. This is discussed in greater detail in ref. [58]. The simulation uses absorbed radiation from the optical model as an input. The simulation divides the meter-long absorber into 50 nodes, and calculates the heat transfer between them. This produces a result for the temperature of the output fluid from the high temperature absorber. This is used to calculate the exergy efficiency according to Equation (2.13). At a direct normal irradiance of  $1000\text{W}/\text{m}^2$  and a photovoltaic cell temperature of  $200^\circ\text{C}$ , the maximum exergy efficiency is 37%.

## 2.5 Considerations for High Temperature Photovoltaics

In this hybrid photovoltaic/thermal system, the photovoltaic cells were designed to operate at 200°C. This allows heat to be collected from the cooling channels behind the cells, but it comes with associated trade-offs. At elevated temperatures, the bandgap of the semiconductor decreases. This produces a corresponding decrease in open circuit voltage. There is also an increase in short circuit current, since a larger portion of the solar spectrum will be absorbed. However, the decrease in voltage has a greater effect than the increase in current, so the efficiency is reduced. Experimental current-voltage (I-V) curves for a GaAs solar cell from Alta Devices under one sun illumination are shown in Figure 21. As

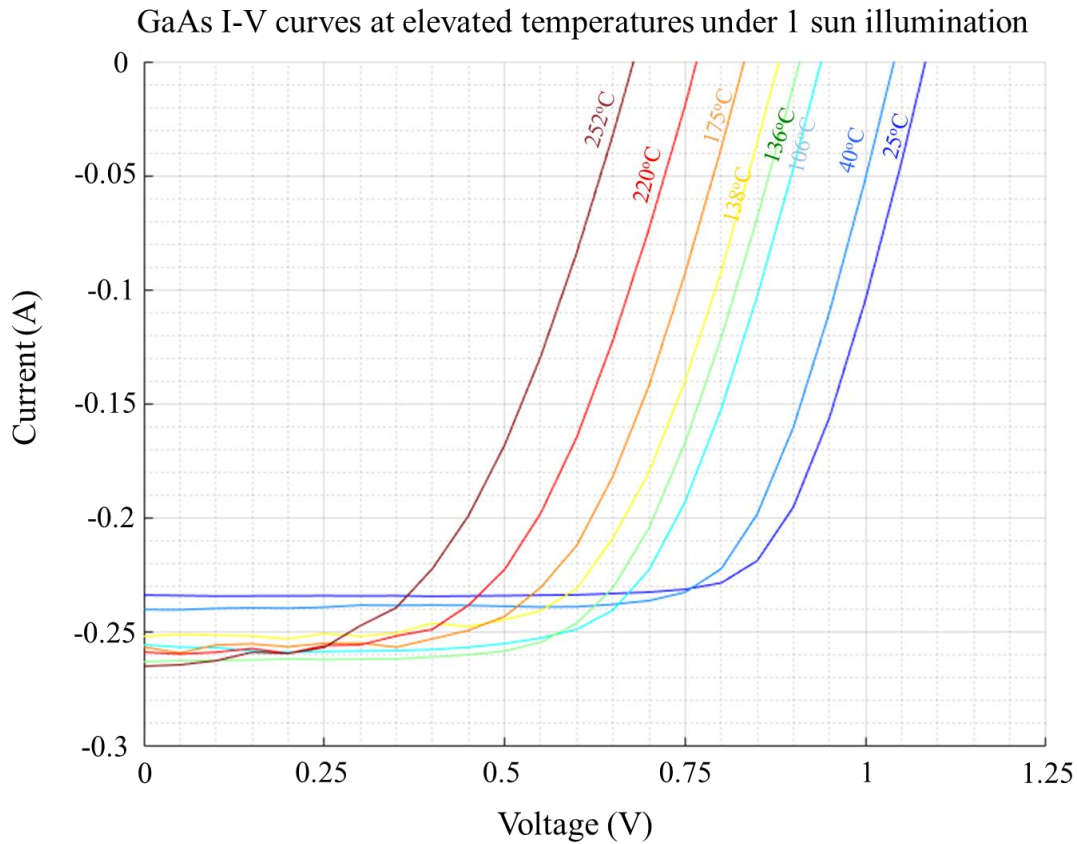


Figure 21 I-V curves for an Alta Devices GaAs solar cell at elevated temperatures under 1 sun illumination. The active area of the cell is 8.53cm<sup>2</sup> in area. Curves shown in reverse polarization, hence the negative current values. As the temperature increases, the semiconductor bandgap decreases. This has the effect of reducing the open circuit voltage, and slightly increasing the short circuit current. As the temperature increased from 25°C to 252°C, the open circuit voltage decreased from 1.08V to 0.68V, and the short circuit current increased from 234mA to 265mA. The cell area was 10cm<sup>2</sup>, so the corresponding short circuit current densities were 23.4mA/cm<sup>2</sup> and 26.5mA/cm<sup>2</sup>. Additionally, the fill factor decreased from 73.6% to 49.7%. Overall the efficiency decreased from 18.6% to 8.9%.

the temperature increased from 25°C to 252°C, the open circuit voltage decreased from 1.08V to 0.68V, and the short circuit current increased from 234mA to 265mA. The cell area was 10cm<sup>2</sup>, but the active area was 8.53cm<sup>2</sup>. The corresponding short circuit current densities were 27.4mA/cm<sup>2</sup> and 31.1mA/cm<sup>2</sup>. Additionally, the fill factor decreased from 73.6% to 49.7%. Overall the efficiency decreased from 21.8% to 10.4%. The initial efficiency differs from the nominal efficiency of 25% due to the series resistance of the contacts, and individual variation in device quality.

In addition to the temporary drops in efficiency discussed above, permanent drops in efficiency can also occur when operating photovoltaics at high temperatures. Two experiments were conducted with a GaAs photovoltaic cell kept under 10 sun illumination at elevated temperatures for one week at a time.

In the first long-term experiment, an Alta Devices GaAs cell was kept at 100°C under 10 sun illumination for 8 hours a day for 5 days. By the end of the experiment, the open circuit voltage and short circuit current remained the same, but the fill factor under 1 sun illumination had degraded by 3%. The 1 sun I-V curves before and after the experiment are shown in Figure 22(a). This can be attributed to an increase in series resistance. The effect in this case was relatively minimal.

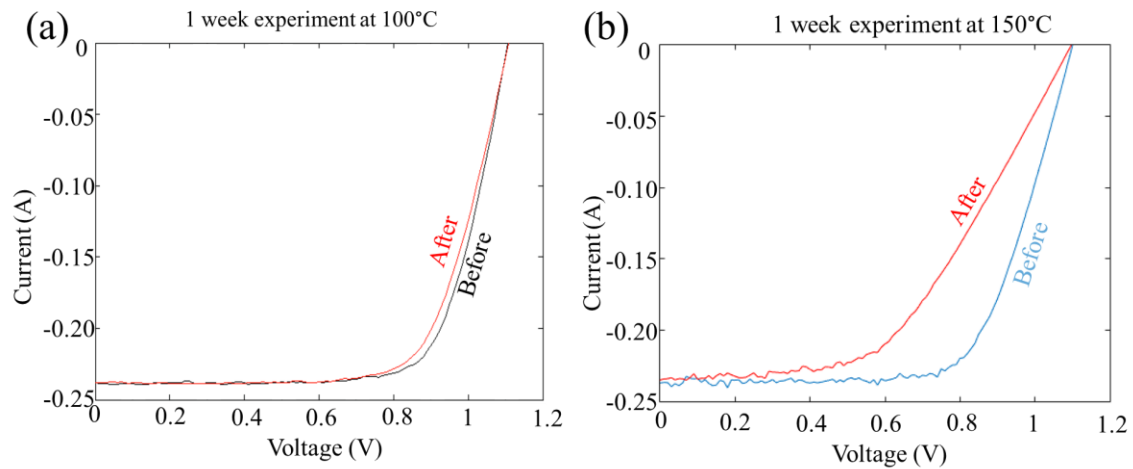


Figure 22 Long-term experiments with an Alta Devices GaAs solar cell at elevated temperatures. (a) In this experiment, the cell was kept at 100°C under 10 sun illumination for 8 hours a day for 5 days. By the end of the experiment, the open circuit voltage and short circuit current remained the same, but the fill factor under 1 sun illumination had degraded by 3%. The 1 sun I-V curves before and after are shown here. (b) In this experiment, the same cell was kept at 150°C under 10 sun illumination for 8 hours a day for 5 days. By the end of the experiment, the open circuit voltage and short circuit current remained the same, but the fill factor under 1 sun illumination had degraded by an additional 28%. The 1 sun I-V curves before and after are shown here.

In the second long-term experiment, the same GaAs cell was kept at 150°C under 10 sun illumination for 8 hours a day for 5 days. By the end of the experiment, the open

circuit voltage and short circuit current remained the same, but the fill factor under 1 sun illumination had degraded by an additional 28%. The 1 sun I-V curves before and after the experiment are shown in Figure 22(b). This again is attributable to an increase in series resistance.

The results of these long-term experiments highlights a challenge for any system that keeps photovoltaic cells operating at elevated temperatures. More research will need to be devoted to semiconductors and bonding materials whose resistance does not change when exposed to heat.

## 2.6 Experimental Results

Results are presented here from an experiment conducted on March 27, 2015. Results for the thermal efficiency of the high temperature absorber at different output temperatures are shown in Figure 23. The thermal efficiency,  $\eta_{\text{solar-thermal}}$ , is the percentage of direct normal incident light on the primary reflector that is converted into useable heat in the high temperature absorber. At the maximum output temperature of 365°C,  $\eta_{\text{solar-thermal}}$  is 37%. Most other data points are near this efficiency. At the output temperature of 330°C, there

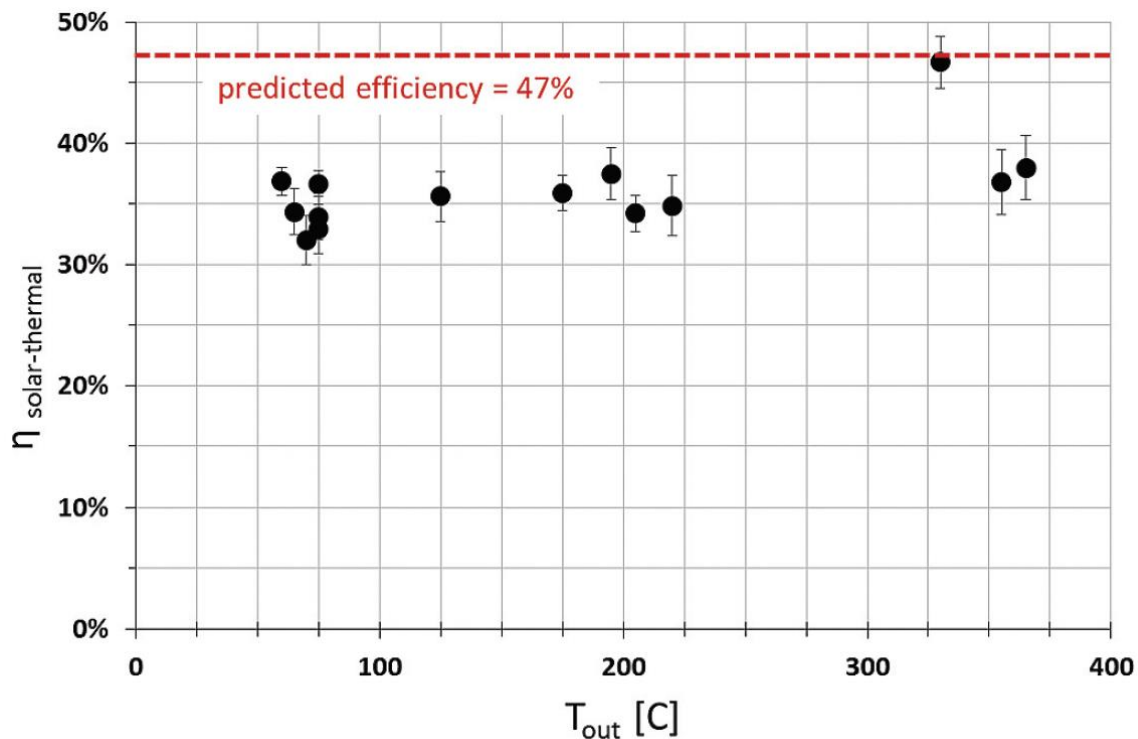


Figure 23 Thermal efficiency for the high temperature absorber. The thermal efficiency,  $\eta_{\text{solar-thermal}}$ , is the percentage of direct normal incident light on the primary reflector that is converted into useable heat in the high temperature absorber. At the maximum output temperature of 365°C,  $\eta_{\text{solar-thermal}}$  is 37%. Most other data points are near this efficiency.

At the output temperature of 330°C, there is an anomalous data point at the predicted efficiency of 47%.

is an anomalous data point that matches the predicted efficiency of 47%. The uncertainty in efficiency calculations is around  $\pm 2\%$ .

The maximum direct electrical efficiency of the photovoltaic cells was obtained on March 20, 2015 under cloudy conditions. The efficiency was around 8%. This low efficiency is partially due to the front grid that was non-ideal for the conditions in which the cell was used. The grid was designed for use under 1 sun illumination. The cell was used inside a concentrator with an illumination intensity of 10 suns. This increases the current, which increases the effect of series resistance. Future work necessitates a cell with a more suitable grid.

A challenge encountered in implementing this system was maintaining adequate solar tracking for optimal illumination in the solar concentrator. The elevation tracker failed during the experiment, so full illumination was only achieved at a specific time each morning. To account for this, all thermal power and efficiency calculations elevation corrected to normalize to full illumination of the receiver tube.

## 2.7 Conclusion

A double-stage hybrid photovoltaic/thermal concentrated solar energy system has been designed, simulated, fabricated, and tested. A non-imaging, 5 meter wide parabolic reflector is used to concentrate sunlight onto a secondary reflector with gallium arsenide (GaAs) photovoltaic cells. These photovoltaic cells convert part of the spectrum directly to electricity, and reflect most of the remainder onto a high temperature absorber. This is made possible by the highly efficient back reflector on the photovoltaic cells, which is also responsible for maximizing the luminescence efficiency, and therefore overall efficiency of the cells. The cells are also actively cooled to provide low-grade heat, further increasing the energy output of the system. The total simulated exergy (useable energy output) efficiency of the system is 37%.

A number of challenges were encountered in the process of implementing the system, and will guide future work. The photovoltaic cells were designed to operate in the system at a temperature of 200°C. However, modelling and experimentation indicates that this adds little to the useable energy output, while greatly increasing system complexity. Reliability and durability issues with the photovoltaic cells are introduced that could be avoided with a lower operating temperature. A maximum photovoltaic efficiency of around 8% was observed experimentally. This can be improved with a denser front contact grid that reduces series resistance, and makes the cell more suitable for the concentrated sunlight of 10 suns that illuminates the cells.

Another challenge encountered when implementing this system was maintenance of output temperature from the high temperature absorber. Due to the properties of the thermal transfer fluid, Therminol VP-1, a maximum outlet temperature of 365°C was reached, which is significantly lower than the target temperature of 500°C. This was also partially due to an imperfect vacuum achieved in the vacuum chamber surrounding the

absorber. In future work, new heat transfer fluids will need to be explored to achieve the desired performance.

Altogether, this hybrid photovoltaic/thermal system was demonstrated, with some recommended modifications for future systems. Such a system using photovoltaic cells at a low temperature, more functional tracking and vacuum systems, and an optimized heat transfer fluid provides a promising technology for achieving the target exergy efficiency of 37%. A large portion of the energy output is heat that can be stored for later energy conversion.

## 4 Theory of Thermo-Photovoltaics

### 4.1 From Dyson Spheres to Thermo-Photovoltaics

Solar energy has become an important and growing industry in recent years. Solar energy is the most plentiful energy source available on earth. A year's worth of sunlight incident on Earth contains  $1.5 \times 10^{18}$  kWh of energy [59]. This is 173 times greater than the energy available in the Earth's combined supply of coal, oil, and gas.

Extrapolating from this, one can imagine a system to capture all the sun's energy with photovoltaics. A system to capture all energy from a star was hypothesized by Freeman Dyson in 1960 [60]. Dyson hypothesized advanced extraterrestrial civilizations may be unobservable by radio or visible radiation. This is because such advanced civilizations could have exceedingly large energy needs, to the point where they would consume most energy output from a star. This could be accomplished with a shell built around the star to consume all the radiation. This concept is commonly referred to as a "Dyson sphere".

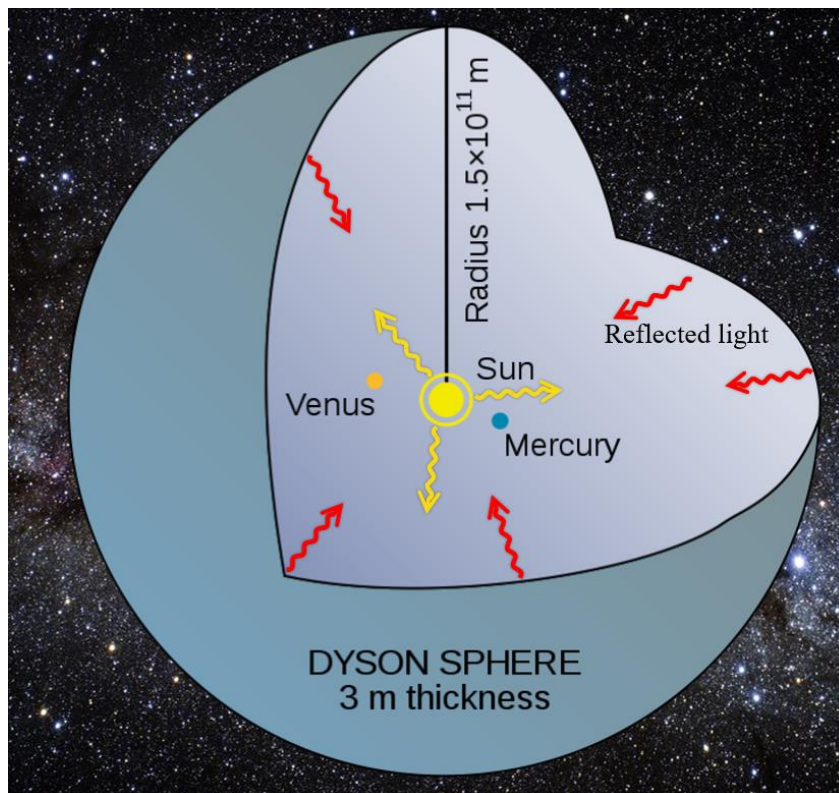


Figure 24 An example of a Dyson sphere. Here, the radius of the sphere is one astronomical unit, equal to  $\sim 1.5 \times 10^{11}$  m. The sun emits a full black body spectrum at a temperature of 5777 Kelvin, and the portion of the spectrum below the bandgap of the photovoltaic cells is reflected back to the sun.

A graphic illustrating the Dyson sphere concept is shown in Figure 24. The theoretical efficiency of such a system can be estimated if photovoltaic cells are used on the interior of the shell to harvest the energy.

While Dyson spheres are still firmly in the realm of science fiction, a miniature version is in the realm of feasible engineering, and is the subject of this chapter. This miniature version of a Dyson sphere is a thermo-photovoltaic system with reflective spectral control, as depicted in Figure 25. This system uses a hot black body emitter that can be heated by combustible fuel [61], concentrated sunlight [62], or nuclear power [63]. This hot emitter is placed inside a vacuum chamber. Photovoltaic cells lining the walls of the chamber collect light from the emitter. For high efficiency, highly reflective photovoltaic cells are used. They reflect unused radiation back to the emitter so the energy is not lost.

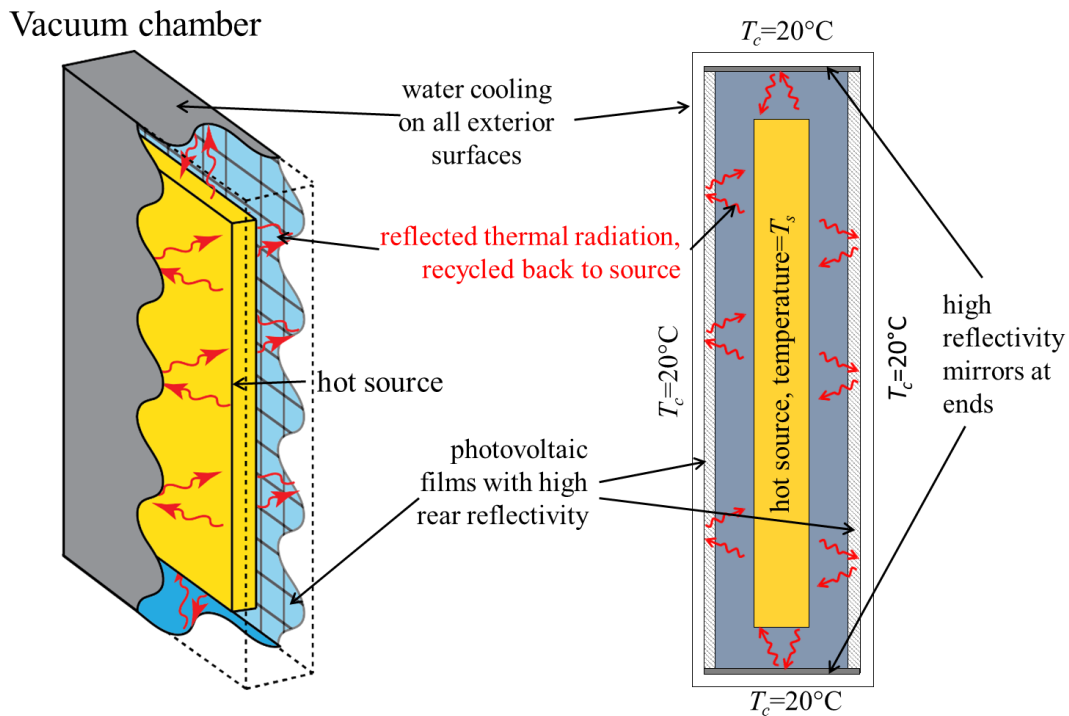


Figure 25 Thermo-photovoltaic system with reflective spectral control. In this system, a hot black body emitter is surrounded by a vacuum chamber. Photovoltaic cells lining the walls of the chamber collect light from the emitter. For high efficiency, highly reflective photovoltaic cells are used. They reflect unused radiation back to the emitter so the energy is not lost.

A visual representation of how the blackbody spectrum from the emitter in such a thermo-photovoltaic system is used is shown in Figure 26. Most of the spectrum is reflected, as depicted in pink. Some of the below-bandgap radiation is parasitically absorbed by the rear mirror, as shown in the orange region labeled “mirror losses”. Most of the above-bandgap radiation is available for conversion to electricity, as shown in the blue region labeled “photovoltaic power”. If no anti-reflection coating is used, some of the above-bandgap radiation will be reflected. This is tolerable in the thermo-photovoltaic system, as this reflected radiation is also not counted as a loss. The semiconductor bandgap depicted in Figure 26 is relatively high for the blackbody spectrum shown. This is a good strategy for high efficiency in this system, as a relatively high bandgap minimizes thermalization losses from high-energy photons.

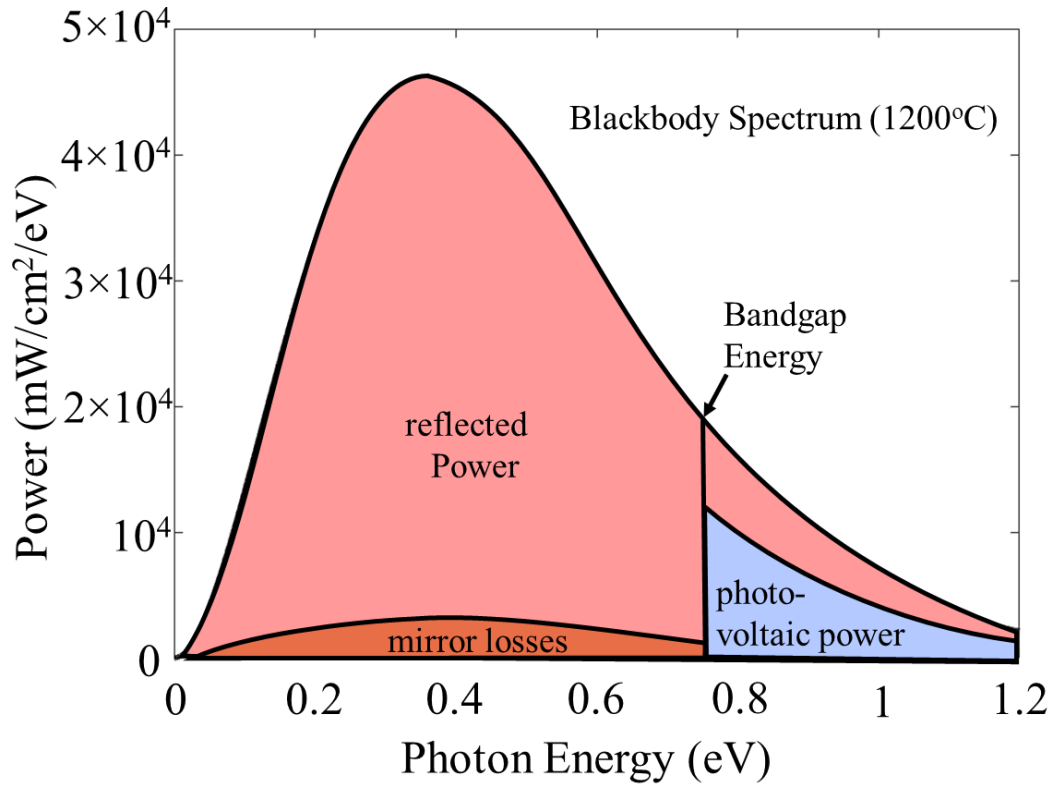


Figure 26 A visual representation of how the blackbody spectrum is used in a thermo-photovoltaic system with highly reflective photovoltaics. Most of the spectrum is reflected, as depicted in pink. Some of the below-bandgap radiation is parasitically absorbed by the rear mirror, as shown in the orange region labeled “mirror losses”. Most of the above-bandgap radiation is available for conversion to electricity, as shown in the blue region labeled “photovoltaic power”. If no anti-reflection coating is used, some of the above-bandgap radiation will be reflected.

## 4.2 Theoretical Efficiency

For a Dyson sphere, or a thermo-photovoltaic system, the spectrum emitted by the emitter/star is given by

$$b_S(E) = \frac{2\pi E^2}{c^2 h^3 \left( \exp\left(\frac{E}{k_B T_S}\right) - 1 \right)} \quad (4.1)$$

Where  $b_S(E)$  is blackbody radiation in units of photons/time/area/energy,  $E$  is the photon energy,  $c$  is the speed of light,  $h$  is Planck’s constant,  $k_B$  is the Boltzmann constant, and  $T_S$  is the temperature of the emitter/star. The short circuit current density of a photovoltaic cell is given by

$$J_{SC} = q \int_0^{\infty} A(E)b_S(E)dE = q \int_{E_g}^{\infty} b_S(E)dE \quad (4.2)$$

where  $q$  is the charge of an electron, and  $A(E)$  is the absorptivity spectrum of the photovoltaic cell, which is taken to be a step function. The black body spectrum of the cell in the dark is given by

$$b_C(E) = \frac{2\pi E^2}{c^2 h^2 \left( \exp\left(\frac{E}{k_B T_C}\right) - 1 \right)} \quad (4.3)$$

where  $T_C$  is the temperature of the photovoltaic cell. The dark saturation current density is given by

$$J_0 = \frac{q}{\eta_{ext}} \int_0^{\infty} A(E)b_C(E)dE = \frac{q}{\eta_{ext}} \int_{E_g}^{\infty} b_C(E)dE \quad (4.4)$$

where  $\eta_{ext}$  is the external luminescence efficiency. The current-voltage relationship for the photovoltaic cell is given by

$$J(V) = J_{SC} - J_0 \exp\left(\frac{V}{k_B T_C}\right) = q \int_{E_g}^{\infty} b_S(E)dE - \frac{q}{\eta_{ext}} \exp\left(\frac{V}{k_B T_C}\right) \int_{E_g}^{\infty} b_C(E)dE \quad (4.5)$$

where  $V$  is the voltage of the photovoltaic cell. This formula assumes perfect carrier collection at the electrodes of the cell.

In a photovoltaic cell, only photons with an energy above the bandgap are absorbed. To improve the efficiency of the Dyson sphere, it is desirable to reflect the unused below-bandgap photons back to the star. This way, the energy in the low-energy photons is not lost, and can be re-used. The efficiency of a system employing this idea can be expressed as the electrical power out as a fraction of the power absorbed by the photovoltaic cells, or

$$\eta = \frac{J_{MPPT} V_{MPPT}}{P_{absorbed}} \quad (4.6)$$

where  $J_{MPPT}$  and  $V_{MPPT}$  are the current density and voltage at the maximum power point on the current-voltage curve.  $P_{absorbed}$  is given by

$$P_{absorbd} = \int_0^{E_g} (1 - Ref(E)) b_{S,power}(E) dE, \quad (4.7)$$

where  $Ref(E)$  is the reflectivity spectrum of the photovoltaic cell. The black body radiation from the star in power/area/energy is represented by  $b_{S,power}$ . It is given by

$$b_{S,power}(E) = E b_S(E) = \frac{2\pi E^3}{c^2 h^3 \left( \exp\left(\frac{E}{k_B T_S}\right) - 1 \right)}. \quad (4.8)$$

The efficiencies of different Dyson spheres around a star with  $T_S=5777K$  is show in Figure 27. Each data point uses a photovoltaic cell with a bandgap optimized for that cell reflectivity. The efficiencies for thermo-photovoltaic systems with emitter temperatures of  $1200^\circ C$  and  $1500^\circ C$  are shown in Figure 27 and Figure 28, respectively.

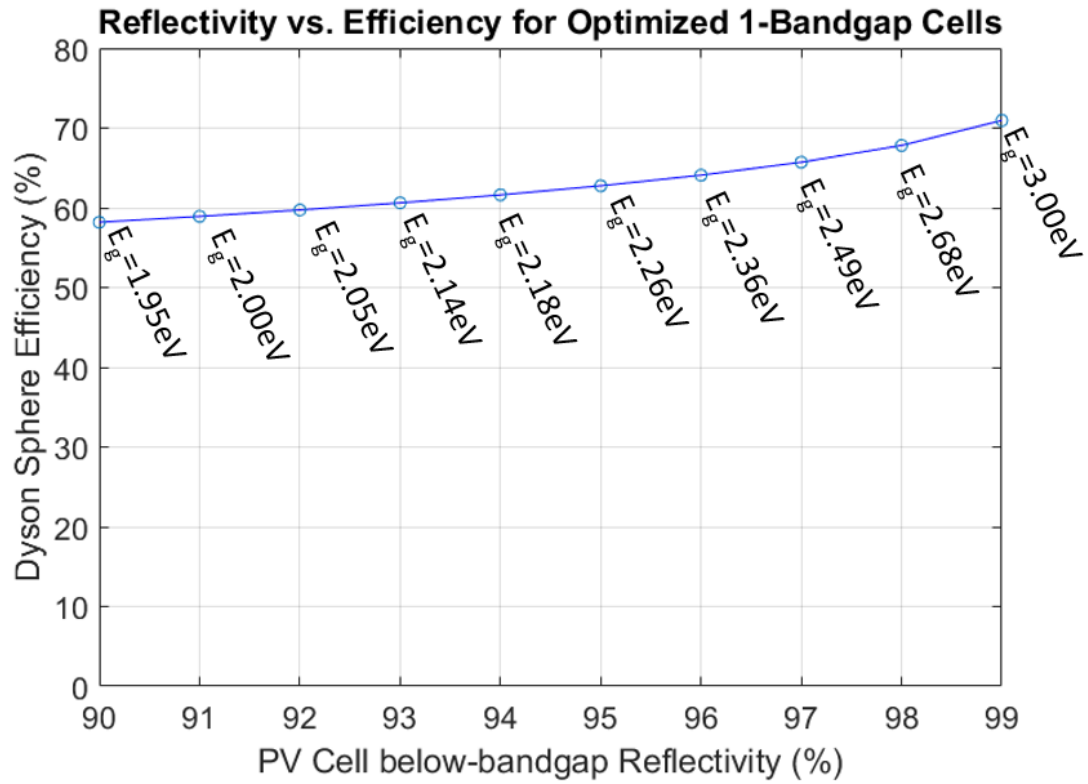


Figure 27 Efficiency verses photovoltaic cell back reflectivity for Dyson spheres. A star temperature of 5777 Kelvin is assumed. A cell temperature of 20°C is assumed. The photovoltaic cell bandgap is optimized for each data point. Efficiency is calculated according to Equation (4.6).

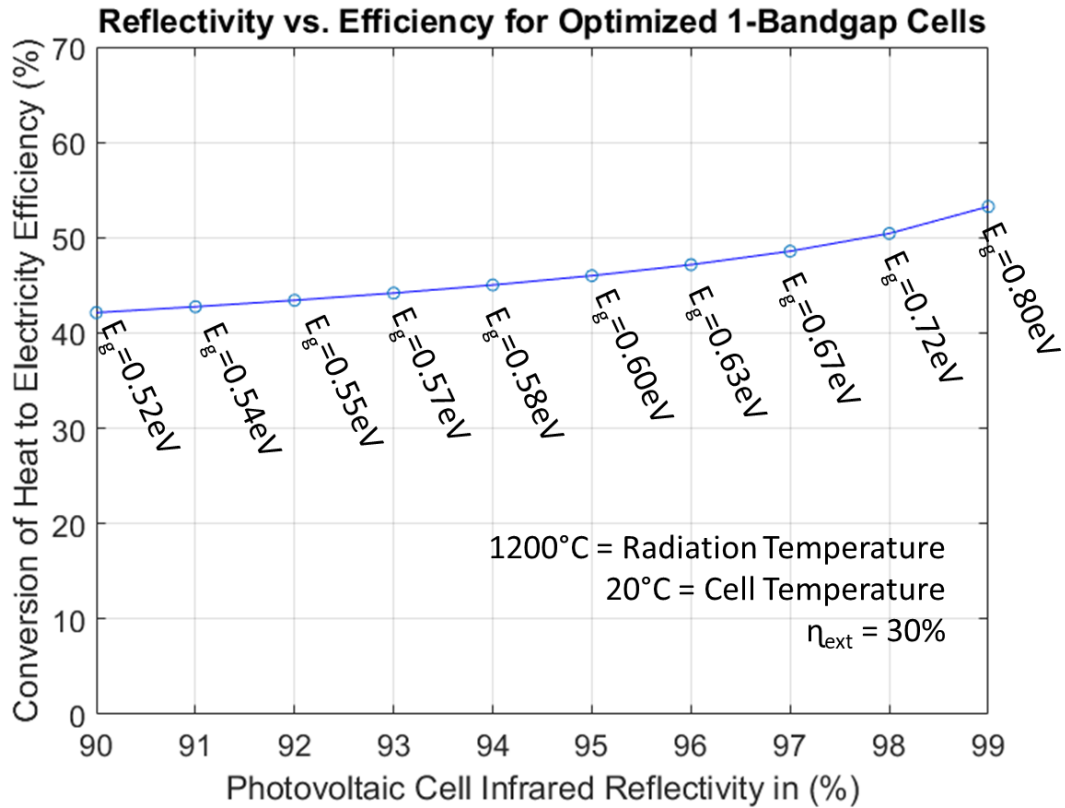


Figure 28 Heat to electricity conversion efficiency for a thermo-photovoltaic system. In this case, the emitter temperature is 1200°C, the cell temperature is 20°C, and the external luminescence efficiency is 30%. The efficiency is 42% at a cell reflectivity of 90%. The efficiency rises above 50% at a cell reflectivity of 98%. The efficiency is 53% at a cell reflectivity of 99%.

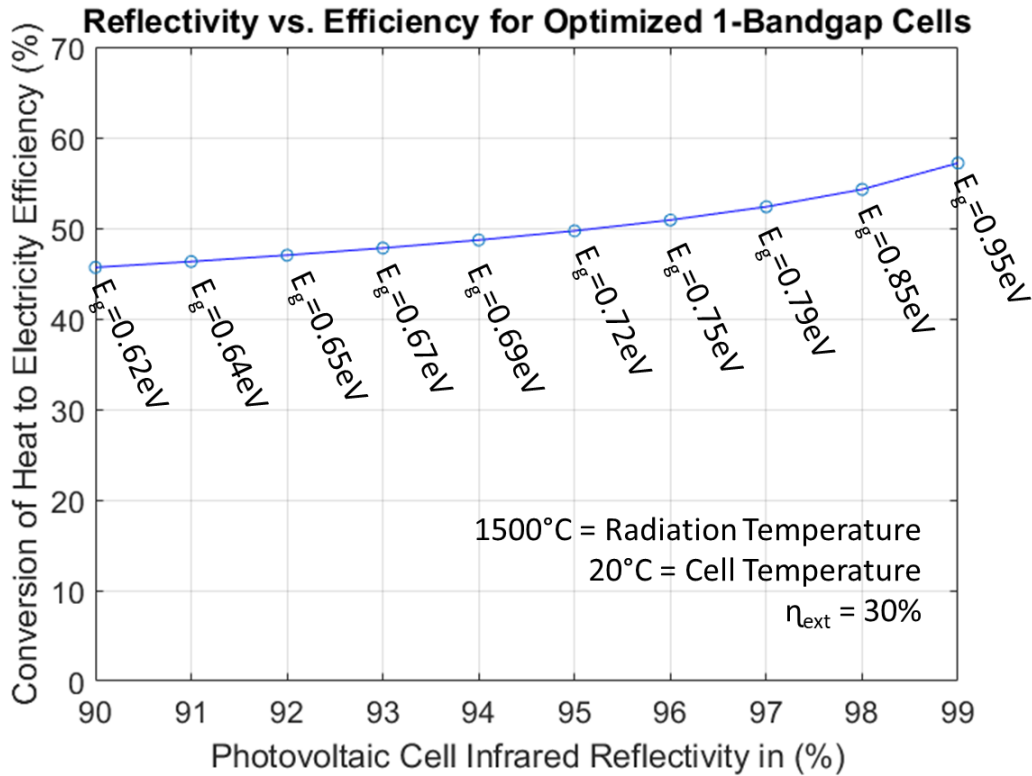


Figure 29 Heat to electricity conversion efficiency for a thermo-photovoltaic system. In this case, the emitter temperature is 1500°C, the cell temperature is 20°C, and the external luminescence efficiency is 30%. The efficiency is 46% at a cell reflectivity of 90%. The efficiency rises to 50% at a cell reflectivity of 95%. The efficiency is 57% at a cell reflectivity of 99%.

### 4.3 History of Thermo-Photovoltaics

The idea of thermo-photovoltaics was established in 1956 [64]. At this time, the inefficiency of photovoltaic cells, especially those with a sufficiently low bandgap, prevented the idea from being pursued intensely. In the 1990s, low bandgap III-V photovoltaic materials, such as GaSb, became available, and interest in thermo-photovoltaics was renewed [61].

Efforts began in the 2000s to design a spectrally selective photonic crystal emitter [65]. This is a strategy for achieving high efficiency that contrasts from the strategy presented in this dissertation. Rather than controlling the spectrum with the reflectivity of the photovoltaic cell, the emissivity spectrum of the emitter is modified. In this strategy, a photonic crystal emitter is designed that suppresses the emission of photons below the bandgap of the photovoltaic material, while allowing emission above the bandgap. It is difficult, however, to achieve high efficiency with this strategy. For instance, in an effort from 2013 to design a 2D tantalum photonic crystal emitter resulted in 30% emissivity in the below-bandgap region [66]. This is analogous to a photovoltaic rear reflector with a reflectivity of 70%, which would result in a much lower efficiency than any data point in Figure 28 or Figure 29. The photonic crystal also needs to be stable high temperatures,

which is difficult for structures with features at the micrometer or nanometer length scale. It has also been proposed to use a bulk refractory metal such as titanium nitride (TiN) as the emitter [67]. However, TiN has an emissivity of 30% for low energy infrared photons [68].

The strategy presented in this dissertation of using a rear reflector behind the photovoltaic cell was recognized in ref. [69]. This avoids the problems of requiring a nanostructure to be stable at high temperatures, or a refractory metal. The band edge of the semiconductor is already a perfect filter of the incoming radiation spectrum. This principle was demonstrated with silicon photovoltaic cells in refs. [70], [71]. In ref. [70] an efficiency of 29% was achieved at an emitter temperature of 2300 K. This strategy was also demonstrated by Bechtel Bettis Inc. in refs. [72]–[75]. In ref. [73], an efficiency of 20.6% was achieved using InGaAs cells with a bandgap of 0.6eV, and an emitter at 1058°C. Subsequently, the same authors added a spectral filter on the front of their photovoltaic cells, bringing the efficiency to 23.6% at an emitter temperature of 1039°C [75]. This is the standing world record for thermo-photovoltaic efficiency at emitter temperatures lower than 2000°C.

# 5 Experiments in Thermo-Photovoltaics

## 5.1 Introduction

To demonstrate high efficiency in thermo-photovoltaics, we performed experiments with a hot emitter near to a photovoltaic cell inside a vacuum chamber. The efficiency discussed in this section is the photovoltaic efficiency, assuming unity optical efficiency. That is, it is assumed that would be achieved in a chamber in which all radiation from the emitter reached the cells, and all reflected radiation made its way back to the emitter.

## 5.2 Experimental Procedure

In our experiment, a thin film indium gallium arsenide ( $\text{In}_{0.555}\text{Ga}_{0.445}\text{As}$ ) photovoltaic cell with a bandgap of 0.74eV was used. This bandgap is well suited to an emitter temperature of 1200°C [32]. The cell was fabricated by the Myles Steiner group at the National Renewable Energy Lab (NREL). The black body emitter consists of a ribbon of graphite, heated with Joule heating by passing a large electrical current through it. The configuration used in the experiment is shown in Figure 30. A baffle is placed between the emitter and the photovoltaic cell to control the illuminated area. The cell is attached with thermally conductive epoxy to a calorimeter that cools the cell, keeping it near room temperature, and measures the absorbed power. For our experiment, the baffle was 1.44mm above the cell, the baffle was 1.04mm thick, and the emitter was 1.22mm above the baffle. The entire apparatus is inside a vacuum chamber with a pressure around  $10^{-5}$  Torr.

The structure of the photovoltaic cell is shown in Figure 31 and Table 1. The p-n junction is located near the back of the cell, at the junction of the active layer and the p-selective contact. The n-selective contact and p-selective contact are made of indium phosphide (InP), which has a bandgap of 1.344eV. The front and rear contact layers are heavily doped to allow electrical contact with the gold electrodes.

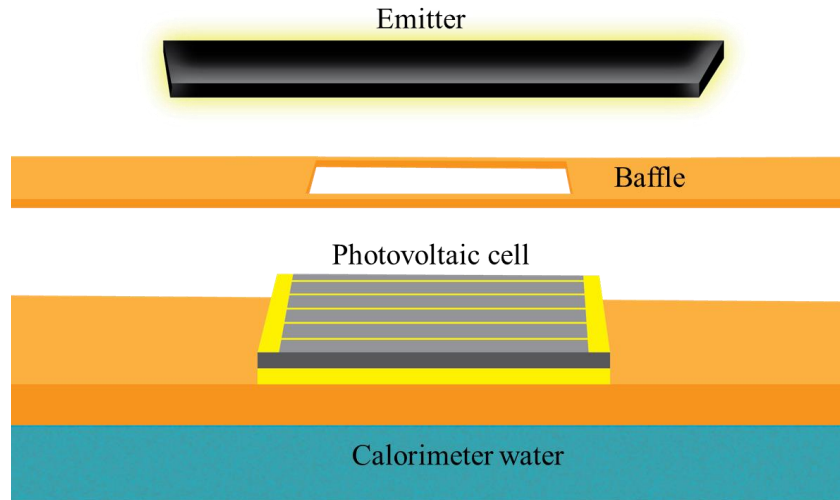


Figure 30 Experimental setup. A planar graphite emitter is heated by passing a large electric current through it. Beneath the emitter, a copper baffle is used to limit the area of the photovoltaic cell exposed to the illumination. The photovoltaic cell is attached to a calorimeter that keeps its temperature steady, while allowing measurements of the heat generated in the cell. For our experiment, the baffle was 1.44mm above the cell, the baffle was 1.04mm thick, and the emitter was 1.22mm above the baffle.

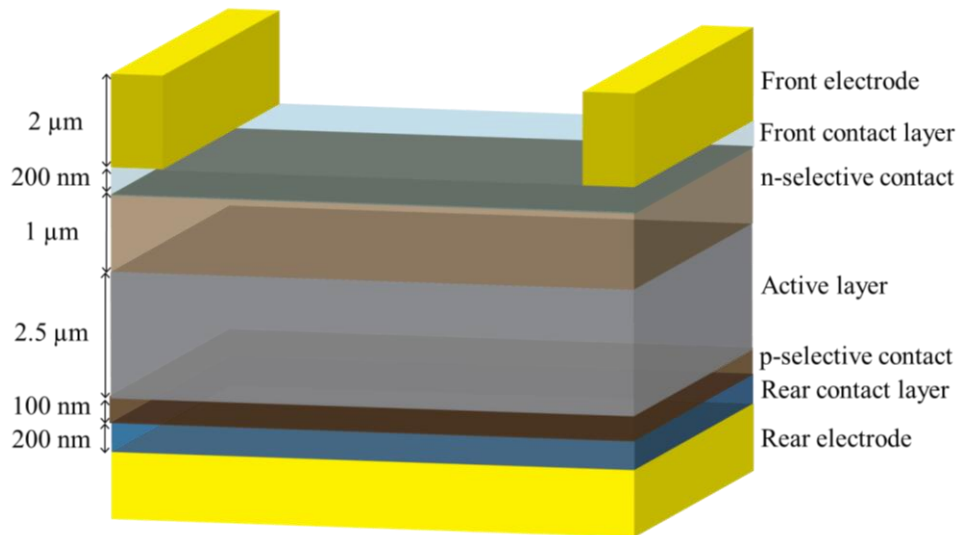


Figure 31 structure of photovoltaic cell. The negative side of the p n junction is on top. The active layer is n doped, and is surrounded by selective contact layers. These are surrounded by highly doped contact layers leading to gold contacts.

layer name	thickness	material	doping
front electrode	2 $\mu\text{m}$	Au	
front contact layer	200 nm	$\text{In}_{0.555}\text{Ga}_{0.445}\text{As}$	n type $10^{18}\text{cm}^{-3}$
n-selective contact	1 $\mu\text{m}$	InP	n type $10^{18}\text{cm}^{-3}$
Active layer	2.5 $\mu\text{m}$	$\text{In}_{0.555}\text{Ga}_{0.445}\text{As}$	n type $3 \times 10^{17}\text{cm}^{-3}$
p-selective contact	100 nm	InP	p type $10^{18}\text{cm}^{-3}$
Rear contact layer	200 nm	InGaAsP	p type $10^{18}\text{cm}^{-3}$
Rear electrode		Au	

Table 1 photovoltaic cell structure. The negative side of the pn junction is on top. The active layer is n doped, and is surrounded by selective contact layers. These are surrounded by highly doped contact layers leading to gold contacts.

The reflectivity of the InGaAs cell used in the experiment is shown in Figure 32(a). This reflectivity spectrum was measured with a Fourier transform infrared (FTIR) spectrometer. The measurement is an average of a range of angles, as the measurement was taken through a microscope objective with a numerical aperture (NA) of 0.65. The below-bandgap reflectivity, averaged over photon energies, is 94%. The above-bandgap reflectivity is 34%, due to Fresnel reflection at the surface of the semiconductor. The external quantum efficiency of the cell is shown in Figure 32(b). The external quantum efficiency is limited to 65% due to Fresnel reflection.

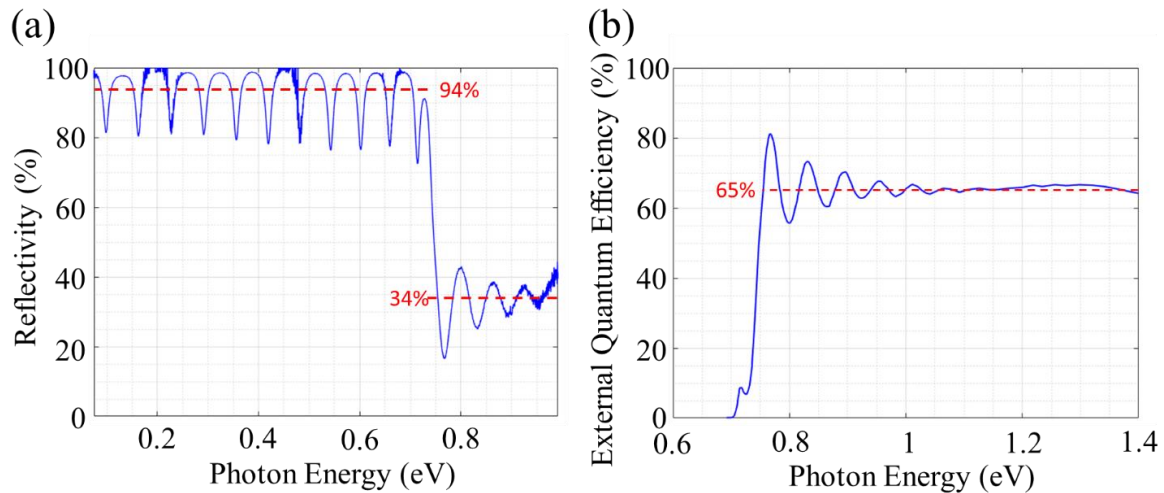


Figure 32 (a) Reflectivity spectrum of the InGaAs cell used in our experiment. This reflectivity spectrum was measured with a fourier transform infrared (FTIR) spectrometer. The measurement is an average over a range of angles, as the measurement was taken through a microscope objective with a numerical aperture (NA) of 0.65. The below-bandgap reflectivity is 94%, and the average above-bandgap reflectivity is 34%, owing to the lack of an anti-reflection coating. (b) External quantum efficiency of the InGaAs cell used in our experiment. The average above-bandgap value is 65%. All measurements are averaged over photon energies.

Data from our experiment is shown in Figure 33 through Figure 35 and Table 2. Sample IV-curves at different emitter temperatures are depicted in Figure 33. The cell has an active area of  $10.04\text{mm}^2$ , and an illuminated area through the baffle of  $4.97\text{mm}^2$ . The electrical power extracted and power absorbed by the cell at different emitter temperatures are shown in Figure 34. The power absorbed is calculated with a modification of Eq. (4.7) that includes the empirical view factor,

$$P_{\text{absorbed}} = AF_{\text{view}} \int_0^{\infty} (1 - \text{Ref}(E)) b_{s,\text{power}}(E) dE, \quad (5.1)$$

and verified with calorimetry (see supplemental information). In this calculation,  $A$  is the cell's active area of  $10.04\text{mm}^2$ . The function  $b_{s,\text{power}}(E)$  is given by Equation (4.8). The function  $\text{Ref}(E)$  is the reflectivity spectrum of the cell, as shown in Figure 32(a). The view factor,  $F_{\text{view}}$ , is a factor that accounts for the limited angular illumination of the cell. The emissivity of the emitter is included inside the view factor. This factor is determined empirically, as described in the following paragraphs.

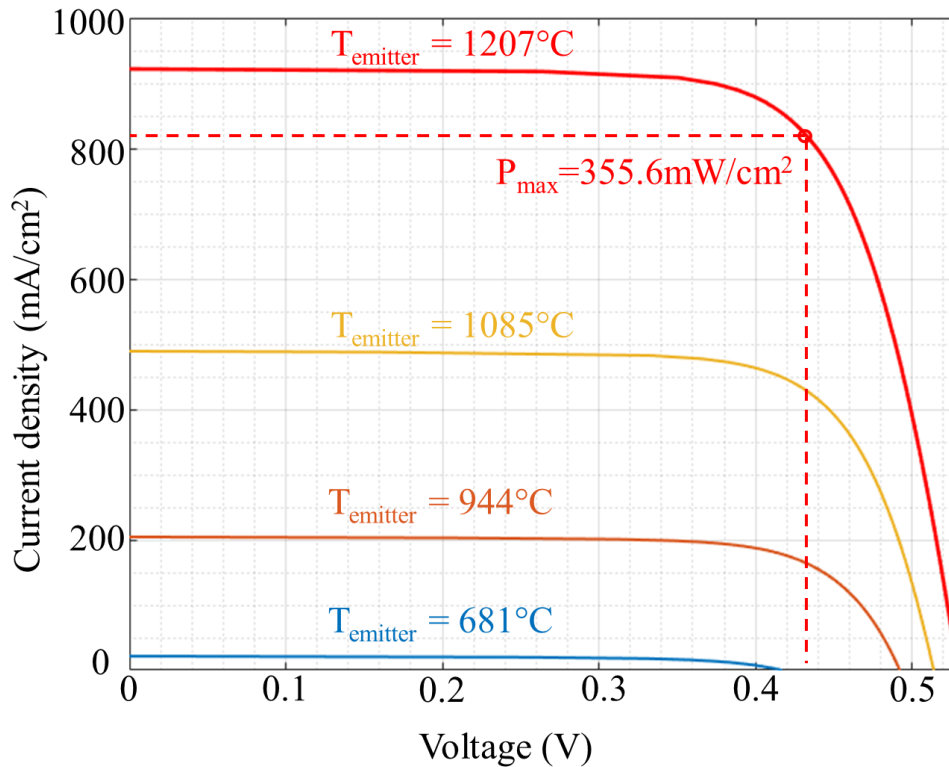


Figure 33 current-voltage curves for the InGaAs cell at different emitter temperatures. The curve for the data point with the highest efficiency is shown in red. The current density is the measured current divided by the cell's active area of  $10.04\text{mm}^2$ .

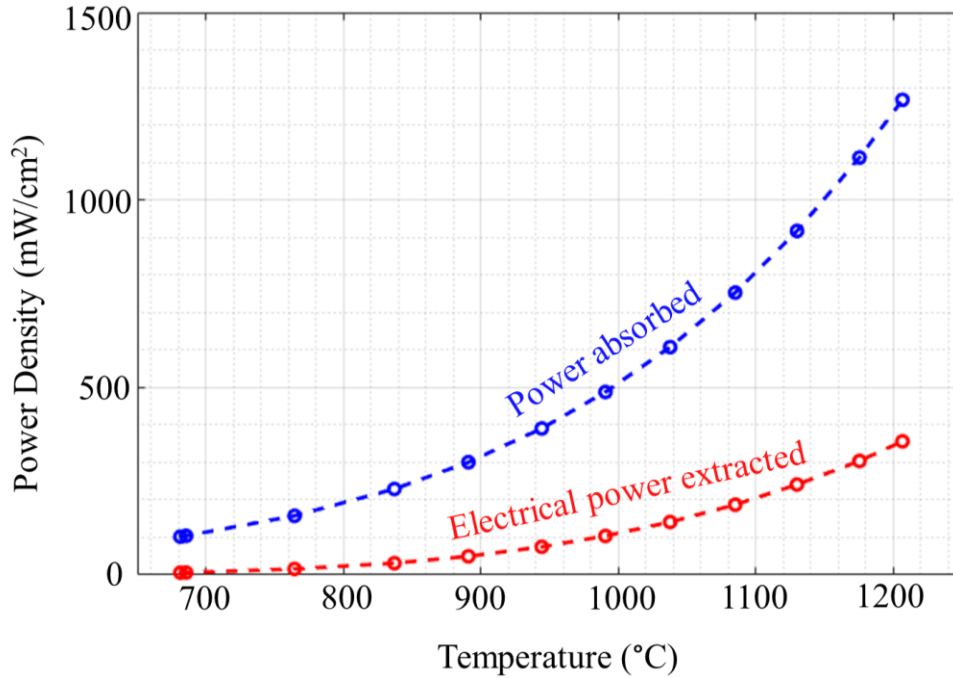


Figure 34 Black body power absorbed by the InGaAs cell (blue), and electrical power extracted from the cell (red). The power absorbed is calculated by multiplying the measured reflectivity of the cell by the black body spectrum for the appropriate emitter temperature and view factor. The multiplied spectrum is then integrated. The power density is the power divided by the cell's active area of  $10.04\text{mm}^2$ .

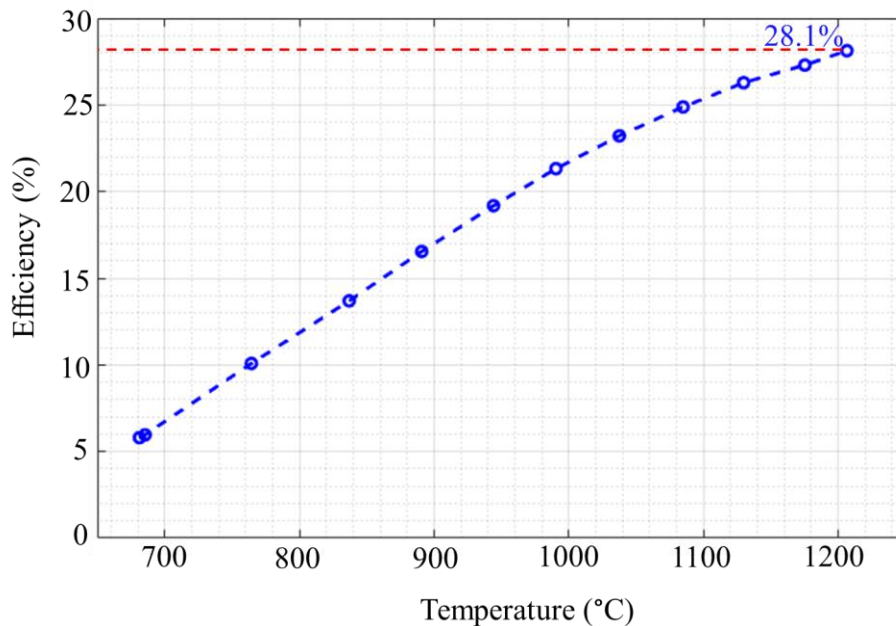


Figure 35 Thermo-photovoltaic efficiency at different emitter temperatures. The maximum efficiency is 28.1% at an emitter temperature of  $1207^\circ\text{C}$ . The efficiency is defined as the electrical power extracted divided by the power absorbed by the cell. This efficiency is given by Equation (4.6) together with Eq (5.1).

emitter temperature (Celcius)	J <sub>SC</sub> (mA/cm <sup>2</sup> )	V <sub>OC</sub> (mV)	Fill Factor (%)	extracted power density (mW/cm <sup>2</sup> )	absorbed power density (mW/cm <sup>2</sup> )	efficiency (%)
681.3	21.61	416.88	65.74	5.88	102.09	5.8
685.5	22.61	418.98	65.76	6.18	104.38	5.9
764.4	49.20	449.86	71.85	15.94	157.77	10.1
837	92.03	468.03	72.87	31.37	229.18	13.7
890.9	139.74	481.22	73.94	49.70	300.50	16.5
944.3	204.38	492.12	74.51	74.70	390.74	19.2
990.6	277.79	500.91	74.76	103.98	487.85	21.3
1038	371.71	507.66	74.75	141.04	607.67	23.2
1085	489.14	513.78	74.54	187.35	752.89	24.9
1130	625.20	518.98	74.3	241.04	917.23	26.3
1175	790.44	523.35	73.46	303.88	1113.14	27.3
1207	921.81	529.2	73.05	356.37	1267.03	28.1

Table 2 Experimental data on electrical characteristics and absorbed power by the photovoltaic cell at different emitter temperatures. The current density, J<sub>SC</sub>, and the power densities are calculated by dividing the current or power by the cell's active area of 10.04mm<sup>2</sup>.

To determine the view factor, we measure the short circuit current of the photovoltaic cell when the emitter is at a known temperature. For this, we place a small copper sample on the emitter, and raise the temperature until it reaches the melting point of copper, at 1085°C. This temperature determines the black body spectrum emitted, and therefore the short circuit current. The short circuit current relates to the view factor by the equation

$$I_{SC} = qAF_{view} \int_0^{\infty} EQE(E) b_S(E) dE, \quad (5.2)$$

where q is the charge of an electron, A is the cell's active area of 10.04mm<sup>2</sup>, F<sub>view</sub> is the view factor, EQE(E) is the external quantum efficiency as shown in Figure 32(b), E is the photon energy, and b<sub>S</sub>(E) is defined in eq (4.1). A plot of measured short circuit current values and their corresponding calculated temperatures are shown in Figure 36. The view factor for our experiment is F<sub>view</sub>=0.302. The view factor is this low, partly due to the fact that the illuminated area is only 4.97mm<sup>2</sup>, and the active area of the cell is 10.04mm<sup>2</sup>.

Efficiency verses emitter temperature is shown in Figure 35. The maximum efficiency reached was 28.1% at an emitter temperature of 1207°C.

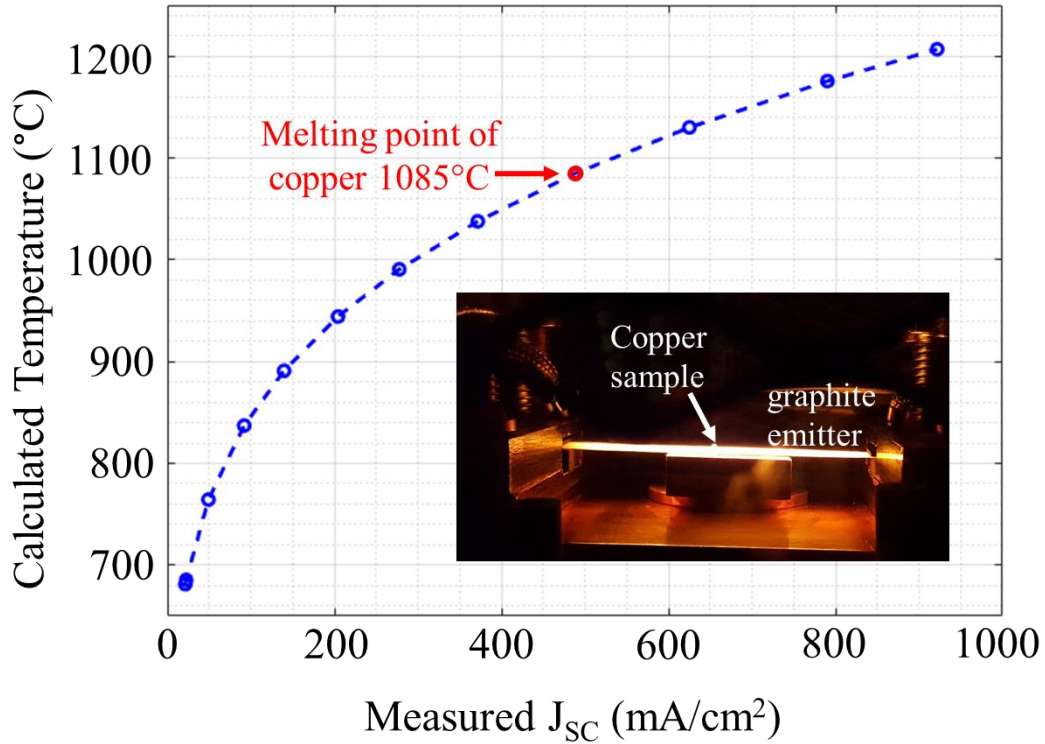


Figure 36 Short circuit current density from photovoltaic cell, and resulting calculated emitter temperature. The emitter temperature was calculated from the cell's short circuit current using Equation (5.2). A small copper sample is placed on top of the emitter. When the copper sample melts, the emitter is at a temperature of 1085°C. This is used to calculate the view factor,  $F_{view}=0.302$ . The current density is the measured current divided by the cell's active area of 10.04mm<sup>2</sup>.

### 5.3 Calorimetry

Calorimetry was performed to verify the power absorbed by the photovoltaic cell. Two separate calorimetry experiments were done for purposes of distinguishing between power absorbed by the cell and excess heat absorbed by the calorimeter. In one experiment, the baffle hole was covered to prevent direct illumination from entering. This is a measurement of the excess heat absorbed by the calorimeter, and is shown as the orange curve in Figure 37.

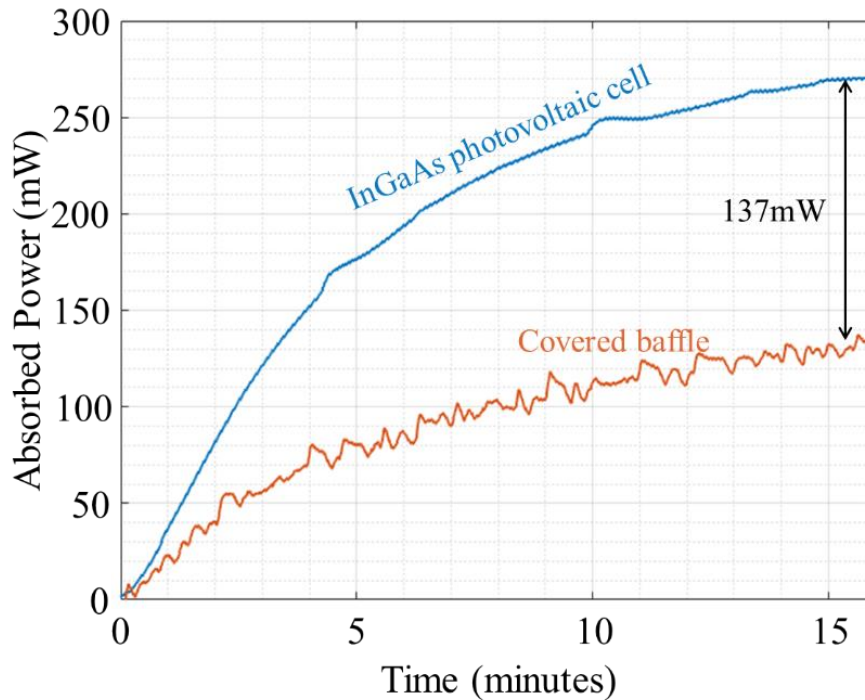


Figure 37 Calorimetry data. Absorbed power is plotted versus time. Absorbed power is calculated with Equation (5.3). Two separate calorimetry experiments were done for purposes of distinguishing between power absorbed by the cell and excess heat absorbed by the calorimeter. In one experiment, the baffle hole was covered to prevent direct illumination from entering (orange). In the other experiment, an open baffle was used with the InGaAs cell (blue). After 15 minutes, the emitter temperature was 1218°C, and the absorbed power by the cell was 137mW (1365mw/cm<sup>2</sup>).

The absorbed power in Figure 37 is calculated by the equation

$$P = \dot{m}c[(T_{out}(t) - T_{out}(0)) - (T_{in}(t) - T_{in}(0))], \quad (5.3)$$

Where  $\dot{m}$  is the mass flow rate of the calorimeter water,  $c$  is the specific heat of water,  $T_{out}(t)$  is the temperature of the outlet water as a function of time, and  $T_{in}(t)$  is the temperature of the inlet water as a function of time. At minute 1 in Figure 37 the temperature of the emitter exceeded 1200°C. At minute 15, the short circuit current of the cell was 101.4mA, corresponding to an emitter temperature of 1218°C, according to Equation (5.2). At this temperature, the absorbed power is 137mW (1365mw/cm<sup>2</sup>), which corresponds to the power measured by calorimetry, as shown in Figure 37. The efficiency remained at 28.1% at the emitter temperature of 1218°C.

#### 5.4 Projections and Future Work

Efficiency data from our experiment versus temperature is shown in Figure 38 in blue, along with a projection. The circles represent empirical data points, and the line represents

the projection. A similar plot for the previous results from Bechtel Bettis Inc. [75] is shown in red in Figure 38.

The projections were made by fitting the IV parameters to the device's experimental data recorded at the emitter temperature of 1207°C. This fit used the equation

$$I = I_{SC} - I_0 \exp\left(\frac{q(V+IR_S)}{nk_B T_C}\right), \quad (5.4)$$

where  $I_{SC}$  is the short circuit current given by Equation (5.2),  $V$  is the voltage,  $n$  is the ideality factor,  $R_S$  is the series resistance, and  $T_C$  is the temperature of the cell. The parameter  $I_0$  is the reverse saturation current. The parameters used for the projection of our data (in blue in Figure 38) are  $R_S=0.47\Omega$ ,  $n=1.2$ , and  $I_0=4.398\text{nA}$  ( $J_0=43.8\text{nA/cm}^2$ ). The maximum projected efficiency is 29.0% at an emitter temperature of 1340°C. The parameters used for the projection of the data from Bechtel Bettis Inc. are  $R_S=0.1\Omega$ ,  $n=1.3$ , and  $I_0=1.55\mu\text{A}$  ( $J_0=11.69\text{mA/cm}^2$ ). The projection for the Bechtel data does not exceed the experimental value of 23.6% at 1039°C.

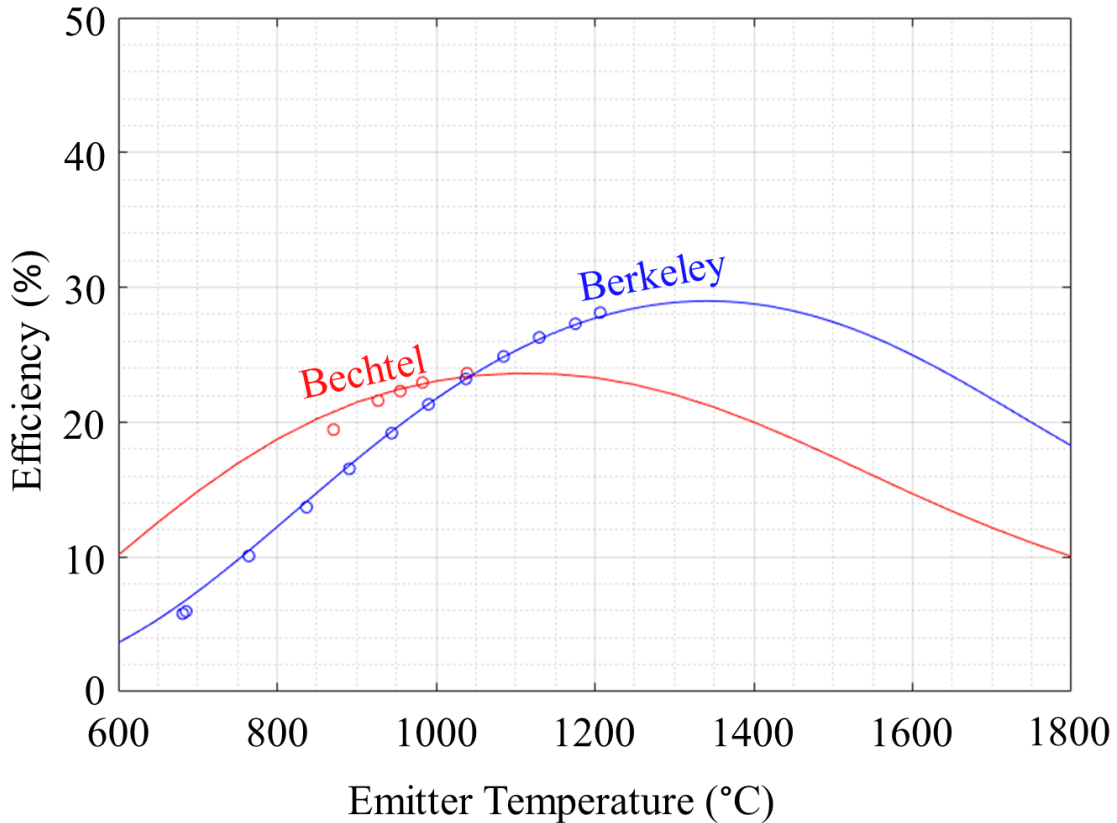


Figure 38 Thermo-photovoltaic efficiency projection for increasing temperature. Experimental values are shown with the circular data points. The fit used for the projection used device parameters that made the best fit to the empirical IV curve. These parameters are a series resistance of  $0.47\Omega$ , an ideality factor of 1.2, and a reverse saturation current of  $I_0=4.398\text{nA}$ .

As seen in Figure 38, the Bechtel data has a higher efficiency at an emitter temperature of 1039°C, but the Berkeley data shows a higher efficiency at higher emitter temperatures. The data point of 28.1% at an emitter temperature of 1207°C is a new world record for thermo-photovoltaic efficiencies at emitter temperatures below 2000°C. A data point at 29% efficiency exists in [70], but this was at an emitter temperature of 2300 Kelvin, and represents a different regime.

Several projections of our data with improved device parameters are shown in Figure 39. The successive curves have successively improving device parameters. The curve labeled “projection using empirical parameters” is the same curve shown in Figure 38. The next curve, labeled “ $R_{\text{Series}}=0.1\Omega$ ”, is a projection that uses the empirical parameters with the series resistance reduced to  $0.1\Omega$ . This has a maximum efficiency of 36% at 1650°C. The curve labeled “Reflectivity=99%” uses the empirical parameters, with the series resistance reduced to  $0.1\Omega$ , and the reflectivity increased to 99%. This has a maximum efficiency of 42.5% at 1435°C. The curve labeled “external luminescence efficiency=30%” uses the empirical parameters, with the series resistance reduced to  $0.1\Omega$ , the reflectivity increased to 99%, the ideality factor set to 1, and the external luminescence efficiency increased to 30%. The external luminescence is related to the reverse saturation current by

$$I_0 = \frac{qAF_{\text{view}}}{\eta_{\text{ext}}} \int_0^{\infty} EQE(E)b_c(E) dE, \quad (5.5)$$

where  $\eta_{\text{ext}}$  is the external luminescence efficiency,  $A$  is the active area of  $10.04\text{mm}^2$ , and  $b_c(E)$  is the black body spectrum emitted by the cell in units of power/area/photon energy, given by eq (4.3). This external luminescence efficiency has been achieved in GaAs cells by Alta Devices, and is also achievable in InGaAs [76]. This has a maximum efficiency of 49.7% at 1385°C. This last curve represents the maximum realistically achievable efficiency with an InGaAs cell in a similar thermo-photovoltaic system.

The projections in Figure 39 show that improvements in the device performance can bring the thermo-photovoltaic efficiency to near-ideal levels, such as those calculated in Figure 28.

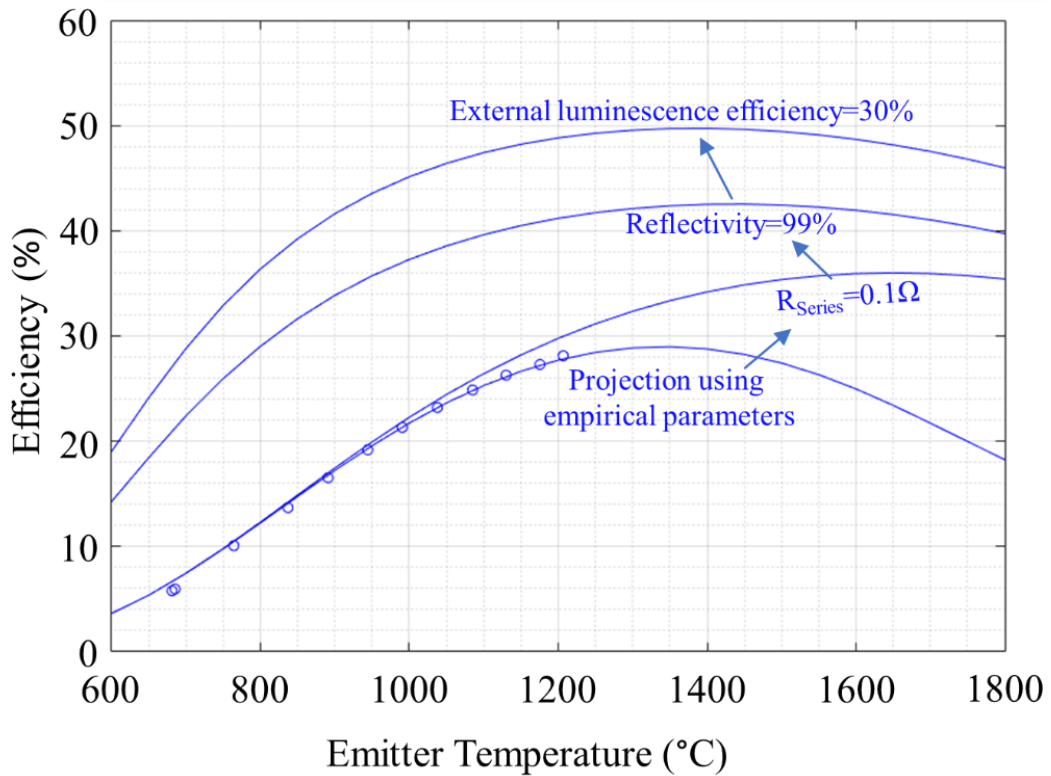


Figure 39 Efficiency projection for increasing temperatures and improved device parameters. The curve labeled “projection using empirical parameters” is the same curve shown in Figure 38. The next curve, labeled “ $R_{Series}=0.1\Omega$ ”, is a projection that uses the empirical parameters with the series resistance reduced to  $0.1\Omega$ . The curve labeled “Reflectivity=99%” uses the empirical parameters, with the series resistance reduced to  $0.1\Omega$ , and the reflectivity increased to 99%. The curve labeled “external luminescence efficiency=30%” uses the empirical parameters, with the series resistance reduced to  $0.1\Omega$ , the reflectivity increased to 99%, and the external luminescence efficiency increased to 30%.

## 6 Conclusion

Several technologies with improved light management for energy efficiency have been demonstrated.

This dissertation has shown that, under a partially coherent source, like a laser, Inverse Lithography Technology can allow EUV Lithography to proceed in spite of severe aberrations, (as would be produced by a single-mirror imaging system). By reducing from 6 mirrors to 1 mirror, the power wasted by the projection optics would be reduced by  $\sim 7\times$ , owing to the diminished mirror losses with fewer mirrors. Since mathematical optimization is needed for mask optimization, the strategy of also using it for aberration correction seems well warranted. We have successfully designed photomasks to print test patterns in the presence of severe spherical aberration and including off-axis coma and astigmatism, and the requirement for 60nm depth of focus. If we force current incoherent EUV sources to produce a six-beam illumination pattern as in Figure 4, the throughput would be very limited. Thus, a partially coherent EUV source, like a laser should warrant more scientific and technological effort.

A double-stage hybrid photovoltaic/thermal concentrated solar energy system has been designed, simulated, fabricated, and tested. A non-imaging, 5 meter wide parabolic reflector is used to concentrate sunlight onto a secondary reflector with gallium arsenide (GaAs) photovoltaic cells. These photovoltaic cells convert part of the spectrum directly to electricity, and reflect most of the remainder onto a high temperature absorber. This is made possible by the highly efficient back reflector on the photovoltaic cells, which is also responsible for maximizing the luminescence efficiency, and therefore overall efficiency of the cells. The cells are also actively cooled to provide low-grade heat, further increasing the energy output of the system. The total simulated exergy (useable energy output) efficiency of the system is 37%. A number of challenges were encountered in the process of implementing the system, and will guide future work. The photovoltaic cells were designed to operate in the system at a temperature of 200°C. However, modelling and experimentation indicates that this adds little to the useable energy output, while greatly increasing system complexity. Reliability and durability issues with the photovoltaic cells are introduced that could be avoided with a lower operating temperature. This hybrid photovoltaic/thermal system was demonstrated, with some recommended modifications for future systems. Such a system using photovoltaic cells at a low temperature, more functional tracking and vacuum systems, and an optimized heat transfer fluid provides a promising technology for achieving the target exergy efficiency of 37%. A large portion of the energy output is heat that can be stored for later energy conversion.

This dissertation reports on a thermo-photovoltaic device that recycles unused radiation from the photovoltaics with a highly reflective rear mirror. Similar to the hybrid photovoltaic/thermal concentrator, this is another technology enabled by record breaking highly reflective photovoltaic cells. Theoretical efficiencies using this strategy are in excess of 50%. In this dissertation, pioneering experimental data has been presented, surpassing previous record-setting results from Bechtel Bettis Inc. As seen in Figure 38,

the Bechtel data has a higher efficiency at an emitter temperature of 1039°C, but the Berkeley data shows a higher efficiency at higher emitter temperatures. The data point of 28.1% at an emitter temperature of 1207°C is a new world record for thermo-photovoltaic efficiencies at emitter temperatures below 2000°C. A data point at 29% efficiency exists in [70], but this was at an emitter temperature of 2300 Kelvin, and represents a different regime. Additionally, theoretical projections have been made for improved device quality. The projections in Figure 39 show that improvements in the device performance can bring the thermo-photovoltaic efficiency to near-ideal levels, such as those calculated in Figure 28.

## References

- [1] H. J. Levinson, *Principles of lithography*, 3rd ed. Bellingham, Wash: SPIE Press, 2010.
- [2] L. Pang, Y. Liu, and D. Abrams, "Inverse Lithography Technology (ILT): what is the impact to the photomask industry?," 2006, p. 62830X.
- [3] Y. Borodovsky, W.-H. Cheng, R. Schenker, and V. Singh, "Pixelated phase mask as novel lithography RET," 2008, p. 69240E.
- [4] P. S. Davids and S. B. Bollepalli, "Generalized inverse problem for partially coherent projection lithography," 2008, p. 69240X.
- [5] V. Singh, B. Hu, K. Toh, S. Bollepalli, S. Wagner, and Y. Borodovsky, "Making a trillion pixels dance," 2008, p. 69240S.
- [6] W.-H. Cheng *et al.*, "Fabrication of defect-free full-field pixelated phase mask," 2008, p. 69241G.
- [7] R. Schenker *et al.*, "Integration of pixelated phase masks for full-chip random logic layers," 2008, p. 69240I.
- [8] G. Kim, J. A. Domínguez-Caballero, and R. Menon, "Design and analysis of multi-wavelength diffractive optics," *Opt. Express*, vol. 20, no. 3, p. 2814, Jan. 2012.
- [9] J. R. Fienup, "Iterative Method Applied To Image Reconstruction And To Computer-Generated Holograms," *Opt. Eng.*, vol. 19, no. 3, Jun. 1980.
- [10] C. Jacobsen and M. R. Howells, "A technique for projection x-ray lithography using computer-generated holograms," *J. Appl. Phys.*, vol. 71, no. 6, pp. 2993–3001, Mar. 1992.
- [11] J. A. Dominguez-Caballero, S. Takahashi, S. J. Lee, and G. Barbastathis, "Design and Fabrication of Computer Generated Holograms for Fresnel Domain Lithography," 2009, p. DWB3.
- [12] Y.-C. Cheng, A. Isoyan, J. Wallace, M. Khan, and F. Cerrina, "Extreme ultraviolet holographic lithography: Initial results," *Appl. Phys. Lett.*, vol. 90, no. 2, p. 023116, Jan. 2007.
- [13] J. S. Jensen and O. Sigmund, "Topology optimization for nano-photonics," *Laser Photonics Rev.*, vol. 5, no. 2, pp. 308–321, Mar. 2011.
- [14] P. Seliger, M. Mahvash, C. Wang, and A. F. J. Levi, "Optimization of aperiodic dielectric structures," *J. Appl. Phys.*, vol. 100, no. 3, p. 034310, Aug. 2006.
- [15] W. R. Frei, D. A. Tortorelli, and H. T. Johnson, "Geometry projection method for optimizing photonic nanostructures," *Opt. Lett.*, vol. 32, no. 1, p. 77, Jan. 2007.
- [16] V. Liu and S. Fan, "Compact bends for multi-mode photonic crystal waveguides with high transmission and suppressed modal crosstalk," *Opt. Express*, vol. 21, no. 7, p. 8069, Apr. 2013.
- [17] G. Veronis, R. W. Dutton, and S. Fan, "Method for sensitivity analysis of photonic crystal devices," *Opt. Lett.*, vol. 29, no. 19, p. 2288, Oct. 2004.
- [18] O. Miller, "Photonic Design: From Fundamental Solar Cell Physics to Computational Inverse Design," PhD, University of California, Berkeley, 2012.

- [19] C. M. Lalau-Keraly, S. Bhargava, O. D. Miller, and E. Yablonovitch, "Adjoint shape optimization applied to electromagnetic design," *Opt. Express*, vol. 21, no. 18, p. 21693, Sep. 2013.
- [20] V. Ganapati, O. D. Miller, and E. Yablonovitch, "Light Trapping Textures Designed by Electromagnetic Optimization for Subwavelength Thick Solar Cells," *IEEE J. Photovolt.*, vol. 4, no. 1, pp. 175–182, Jan. 2014.
- [21] M. P. Bendsøe and O. Sigmund, *Topology Optimization: Theory, Methods, and Applications*. Berlin, Heidelberg: Springer Berlin Heidelberg, 2004.
- [22] G. Strang, *Computational science and engineering*, 2. print. Wellesley, Mass: Wellesley-Cambridge Press, 2012.
- [23] S. Bhargava and E. Yablonovitch, "Multi-objective inverse design of sub-wavelength optical focusing structures for heat assisted magnetic recording," 2014, p. 92010M.
- [24] J. W. Goodman, *Introduction to Fourier optics*, 2nd ed. New York: McGraw-Hill, 1996.
- [25] M. Born and E. Wolf, *Principles of optics: electromagnetic theory of propagation, interference and diffraction of light*, 7th expanded ed. Cambridge ; New York: Cambridge University Press, 1999.
- [26] V. N. Mahajan, *Aberration theory made simple*. Bellingham, Wash., USA: SPIE Optical Engineering Press, 1991.
- [27] S. G. Krantz, *A guide to complex variables*. Washington, D.C.: Mathematical Association of America, 2008.
- [28] Y. Borodovsky, "EUV Lithography at Insertion and Beyond." .
- [29] C. Solomon and T. Breckon, *Fundamentals of digital image processing: a practical approach with examples in Matlab*. Chichester, West Sussex ; Hoboken, NJ: Wiley-Blackwell, 2011.
- [30] M. A. Green, K. Emery, Y. Hishikawa, W. Warta, and E. D. Dunlop, "Solar cell efficiency tables (version 43): Solar cell efficiency tables," *Prog. Photovolt. Res. Appl.*, vol. 22, no. 1, pp. 1–9, Jan. 2014.
- [31] W. Shockley and H. J. Queisser, "Detailed Balance Limit of Efficiency of  $p-n$  Junction Solar Cells," *J. Appl. Phys.*, vol. 32, no. 3, pp. 510–519, Mar. 1961.
- [32] V. Ganapati, "Optical Design Considerations for High Conversion Efficiency in Photovoltaics," PhD, University of California, Berkeley, 2015.
- [33] "Renewable energy sources and climate change mitigation: special report of the Intergovernmental Panel on Climate Change," *Choice Rev. Online*, vol. 49, no. 11, pp. 49-6309-49-6309, Jul. 2012.
- [34] E. C. J. Kern and M. C. Russell, "Combined Photovoltaic and thermal hybrid collector systems," presented at the Conference: IEEE photovoltaic specialists conference, Washington, DC, USA, 1978, p. COO-4577-3; CONF-780619-24.
- [35] N. Aste, G. Chiesa, and F. Verri, "Design, development and performance monitoring of a photovoltaic-thermal (PVT) air collector," *Renew. Energy*, vol. 33, no. 5, pp. 914–927, May 2008.
- [36] P. G. Charalambous, G. G. Maidment, S. A. Kalogirou, and K. Yiakoumetti, "Photovoltaic thermal (PV/T) collectors: A review," *Appl. Therm. Eng.*, vol. 27, no. 2–3, pp. 275–286, Feb. 2007.

- [37] T. T. Chow, "A review on photovoltaic/thermal hybrid solar technology," *Appl. Energy*, vol. 87, no. 2, pp. 365–379, Feb. 2010.
- [38] T. T. Chow, G. N. Tiwari, and C. Menezo, "Hybrid Solar: A Review on Photovoltaic and Thermal Power Integration," *Int. J. Photoenergy*, vol. 2012, pp. 1–17, 2012.
- [39] A. Ibrahim, M. Y. Othman, M. H. Ruslan, S. Mat, and K. Sopian, "Recent advances in flat plate photovoltaic/thermal (PV/T) solar collectors," *Renew. Sustain. Energy Rev.*, vol. 15, no. 1, pp. 352–365, Jan. 2011.
- [40] J. J. Michael, I. S, and R. Goic, "Flat plate solar photovoltaic–thermal (PV/T) systems: A reference guide," *Renew. Sustain. Energy Rev.*, vol. 51, pp. 62–88, Nov. 2015.
- [41] A. Kumar, P. Baredar, and U. Qureshi, "Historical and recent development of photovoltaic thermal (PVT) technologies," *Renew. Sustain. Energy Rev.*, vol. 42, pp. 1428–1436, Feb. 2015.
- [42] R. Kumar and M. A. Rosen, "A critical review of photovoltaic–thermal solar collectors for air heating," *Appl. Energy*, vol. 88, no. 11, pp. 3603–3614, Nov. 2011.
- [43] L. Zhang, D. Jing, L. Zhao, J. Wei, and L. Guo, "Concentrating PV/T Hybrid System for Simultaneous Electricity and Usable Heat Generation: A Review," *Int. J. Photoenergy*, vol. 2012, pp. 1–8, 2012.
- [44] N. Aste, C. del Pero, and F. Leonforte, "Water flat plate PV–thermal collectors: A review," *Sol. Energy*, vol. 102, pp. 98–115, Apr. 2014.
- [45] M. Y. Othman, A. Ibrahim, G. L. Jin, M. H. Ruslan, and K. Sopian, "Photovoltaic–thermal (PV/T) technology – The future energy technology," *Renew. Energy*, vol. 49, pp. 171–174, Jan. 2013.
- [46] K. E. Amori and M. A. Abd-AllRaheem, "Field study of various air based photovoltaic/thermal hybrid solar collectors," *Renew. Energy*, vol. 63, pp. 402–414, Mar. 2014.
- [47] M. Y. Othman, S. A. Hamid, M. A. S. Tabook, K. Sopian, M. H. Roslan, and Z. Ibarahim, "Performance analysis of PV/T Combi with water and air heating system: An experimental study," *Renew. Energy*, vol. 86, pp. 716–722, Feb. 2016.
- [48] O. Rejeb, H. Dhaou, and A. Jemni, "A numerical investigation of a photovoltaic thermal (PV/T) collector," *Renew. Energy*, vol. 77, pp. 43–50, May 2015.
- [49] J. S. Coventry, "Performance of a concentrating photovoltaic/thermal solar collector," *Sol. Energy*, vol. 78, no. 2, pp. 211–222, Feb. 2005.
- [50] A. G. Enecolo and A. G. E. Schweizer, "New Generation of Hybrid Solar PV/T Collectors," *Swiss Fed. Off. Energy*, pp. 1–55.
- [51] E. Skoplaki and J. A. Palyvos, "On the temperature dependence of photovoltaic module electrical performance: A review of efficiency/power correlations," *Sol. Energy*, vol. 83, no. 5, pp. 614–624, May 2009.
- [52] M. Abdelhamid, R. Singh, A. Qattawi, M. Omar, and I. Haque, "Evaluation of On-Board Photovoltaic Modules Options for Electric Vehicles," *IEEE J. Photovolt.*, vol. 4, no. 6, pp. 1576–1584, Nov. 2014.
- [53] M. Abdelhamid, A. Qattawi, R. Singh, and I. Haque, "Comparison of an analytical hierarchy process and fuzzy axiomatic design for selecting appropriate

- photovoltaic modules for onboard vehicle design," *Int. J. Mod. Eng.*, vol. 15, no. 1, pp. 23–35.
- [54] M. Brogren, P. Nostell, and B. Karlsson, "Optical efficiency of a PV–thermal hybrid CPC module for high latitudes," *Sol. Energy*, vol. 69, pp. 173–185, Jul. 2001.
- [55] C. Kong, Z. Xu, and Q. Yao, "Outdoor performance of a low-concentrated photovoltaic–thermal hybrid system with crystalline silicon solar cells," *Appl. Energy*, vol. 112, pp. 618–625, Dec. 2013.
- [56] M. Li, X. Ji, G. Li, S. Wei, Y. Li, and F. Shi, "Performance study of solar cell arrays based on a Trough Concentrating Photovoltaic/Thermal system," *Appl. Energy*, vol. 88, no. 9, pp. 3218–3227, Sep. 2011.
- [57] M. Abdelhamid *et al.*, "Novel double-stage high-concentrated solar hybrid photovoltaic/thermal (PV/T) collector with nonimaging optics and GaAs solar cells reflector," *Appl. Energy*, vol. 182, pp. 68–79, Nov. 2016.
- [58] B. K. Widyolar *et al.*, "Design, simulation and experimental characterization of a novel parabolic trough hybrid solar photovoltaic/thermal (PV/T) collector," *Renew. Energy*, vol. 101, pp. 1379–1389, Feb. 2017.
- [59] P. Würfel and U. Würfel, *Physics of solar cells: from basic principles to advanced concepts*, 2nd, updated and expanded ed ed. Weinheim: Wiley-VCH, 2009.
- [60] F. J. Dyson, "Search for Artificial Stellar Sources of Infrared Radiation," *Science*, vol. 131, no. 3414, pp. 1667–1668, Jun. 1960.
- [61] L. Fraas and L. Minkin, "TPV History from 1990 to Present & Future Trends," 2007, vol. 890, pp. 17–23.
- [62] N.-P. Harder and P. Würfel, "Theoretical limits of thermophotovoltaic solar energy conversion," *Semicond. Sci. Technol.*, vol. 18, no. 5, pp. S151–S157, May 2003.
- [63] V. L. Teofilo, P. Choong, J. Chang, Y.-L. Tseng, and S. Ermer, "Thermophotovoltaic Energy Conversion for Space †," *J. Phys. Chem. C*, vol. 112, no. 21, pp. 7841–7845, May 2008.
- [64] R. E. Nelson, "A brief history of thermophotovoltaic development," *Semicond. Sci. Technol.*, vol. 18, no. 5, pp. S141–S143, May 2003.
- [65] J. M. Gee, J. B. Moreno, Shawn-Yu Lin, and J. G. Fleming, "Selective emitters using photonic crystals for thermophotovoltaic energy conversion," 2002, pp. 896–899.
- [66] Y. X. Yeng, W. R. Chan, V. Rinnerbauer, J. D. Joannopoulos, M. Soljačić, and I. Celanovic, "Performance analysis of experimentally viable photonic crystal enhanced thermophotovoltaic systems," *Opt. Express*, vol. 21, no. S6, p. A1035, Nov. 2013.
- [67] U. Guler, A. Boltasseva, and V. M. Shalaev, "Refractory Plasmonics," *Science*, vol. 344, no. 6181, pp. 263–264, Apr. 2014.
- [68] G. V. Naik, J. L. Schroeder, X. Ni, A. V. Kildishev, T. D. Sands, and A. Boltasseva, "Titanium nitride as a plasmonic material for visible and near-infrared wavelengths," *Opt. Mater. Express*, vol. 2, no. 4, p. 478, Apr. 2012.
- [69] J. J. Werth, "Thermo-photovoltaic converter with radiant energy reflective means," Jul. 1967.

- [70] R. M. Swanson, "Recent developments in thermophotovoltaic conversion," 1980, pp. 186–189.
- [71] R. M. Swanson, "Silicon photovoltaic cells in thermophotovoltaic energy conversion," 1978, pp. 70–73.
- [72] R. G. Mahorter, B. Wernsman, R. M. Thomas, and R. R. Siergiej, "Thermophotovoltaic system testing," *Semicond. Sci. Technol.*, vol. 18, no. 5, p. S232, 2003.
- [73] R. R. Siergiej, "20% Efficient InGaAs/InPAs Thermophotovoltaic Cells," 2003, vol. 653, pp. 414–423.
- [74] B. Wernsman, "Optical Cavity Effects on TPV Efficiency and Power Density," 2003, vol. 653, pp. 277–286.
- [75] B. Wernsman *et al.*, "Greater Than 20% Radiant Heat Conversion Efficiency of a Thermophotovoltaic Radiator/Module System Using Reflective Spectral Control," *IEEE Trans. Electron Devices*, vol. 51, no. 3, pp. 512–515, Mar. 2004.
- [76] V. Ganapati, T. P. Xiao, and E. Yablonovitch, "Ultra-Efficient Thermophotovoltaics Exploiting Spectral Filtering by the Photovoltaic Band-Edge," *ArXiv E-Prints*, Nov. 2016.